

Seasonal and static gravity field of Mars from MGS, Mars Odyssey and MRO radio science

Antonio Genova^{a,b}, Sander Goossens^{c,b}, Frank G. Lemoine^b, Erwan Mazarico^b, Gregory A. Neumann^b, David E. Smith^a, Maria T. Zuber^a

^a*Department of Earth, Atmospheric and Planetary Sciences, Massachusetts Institute of Technology, Cambridge, Massachusetts, USA.*

^b*NASA Goddard Space Flight Center, Greenbelt, Maryland, USA.*

^c*CRESST, University of Maryland/Baltimore County, Baltimore, Maryland, USA.*

Abstract

We present a spherical harmonic solution of the static gravity field of Mars to degree and order 120, GMM-3, that has been calculated using the Deep Space Network (DSN) tracking data of the NASA Mars missions, Mars Global Surveyor (MGS), Mars Odyssey (ODY), and the Mars Reconnaissance Orbiter (MRO). We have also jointly determined spherical harmonic solutions for the static and time-variable gravity field of Mars, and the Mars k_2 Love numbers, exclusive of the gravity contribution of the atmosphere. Consequently, the retrieved time-varying gravity coefficients and the Love number k_2 solely yield seasonal variations in the mass of the polar caps and the solid tides of Mars, respectively. We obtain a Mars Love number k_2 of 0.1697 ± 0.0027 ($3\text{-}\sigma$). The inclusion of MRO tracking data results in improved seasonal gravity field coefficients C_{30} and, for the first time, C_{50} . Refinements of the atmospheric model in our orbit determination program have allowed us to monitor the odd zonal harmonic C_{30} for ~ 1.5 solar cycles (16 years). This gravity model shows improved correlations with MOLA topography up to 15% larger at higher harmonics ($l=60\text{-}80$) than previous solutions.

Keywords: Mars, gravity field, tides, polar caps

2010 MSC: 00-01, 99-00

1. Introduction

Over the past two decades NASA’s Mars Exploration Program made use of orbiters, landers, and rovers to investigate and monitor the planet Mars. The NASA spacecraft Mars Global Surveyor (MGS), 2001 Mars Odyssey (ODY), and Mars Reconnaissance Orbiter (MRO) have contributed to the survey of the planet over the past 16 years. MGS operated between 1999 and 2006, whereas ODY and MRO are still orbiting Mars with various instruments including optical and thermal imaging systems, spectrometers, a subsurface radar, and radio tracking systems.

MGS was designed to be a global mapping mission that examined the whole planet from the atmosphere to the surface. The Mars Orbiter Laser Altimeter (MOLA) was one of the five instruments on board, and it operated only until June 2001. The ranging measurements from the MGS spacecraft to the Martian surface resulted in high-resolution topographic maps of the planet (Smith et al., 1999b), that are still the most geodetically accurate. The comparison of these topographic maps with a model of Mars gravity provides information on the interior structure and thermal evolution of the planet (Zuber et al., 2000). The current global topography has a resolution of 1 km in latitude and 2 km in longitude at the equator (Smith et al., 2001), therefore, an improved resolution of the gravity field is needed to determine in detail the mantle and crust formation and structure.

MGS, ODY, and MRO were all located in mapping orbits for their primary mission phases at different altitudes and Local Solar Times (LST) (Cutting et al., 1978). The NASA Deep Space Network (DSN) stations have acquired X-Band tracking data from these spacecraft that provide information on the static and time-varying gravity field of Mars. The continuity of the radio tracking data, which cover more than an entire solar cycle, is a unique opportunity to also characterize the temporal variability of the gravity field, relevant to the planet’s internal dynamics and the structure and dynamics of the atmosphere (Zuber et al., 2007). Data from other mission phases at lower altitudes (< 250 km) also

help improve the resolution of the static gravity field. MGS Science Phasing Orbit (SPO) 1 and 2, ODY Transition orbit (ODYT), and MRO Transition orbit (MROT) had periapsis altitudes between 170 and 220 km.

Radio science investigations for global high-resolution gravity fields of Mars were conducted with MGS, providing spherical harmonics up to degree and order 75, which corresponds to a spatial resolution of ~ 140 km (Smith et al., 1999a; Lemoine et al., 2001; Yuan et al., 2001). Mars Odyssey tracking data allowed to improve the resolution of the static gravity up to ~ 110 km, and the measurement of the seasonal changes in the gravity caused by the mass exchange between polar ice caps and atmosphere (Konopliv et al., 2006; Marty et al., 2009). MRO contributed to refining the Mars gravity field model. The lower altitude of the spacecraft enabled Konopliv et al. (2011) to recover a high-resolution gravity field model of the planet to degree and order 110 (spatial resolution of ~ 96 km). The latest solution, which is also a 110^{th} degree and order spherical harmonic model called MRO110C, was released on the NASA Planetary Data System (PDS) by the Jet Propulsion Laboratory (JPL) in 2012 (Konopliv, 2012). The tracking data used to determine this field included: MGS SPO 1 and 2, Gravity Calibration Orbit (GCO), and Mapping Orbit (MAP) until November 2006; ODYT, and ODY Mapping Orbit (ODYM) until December 2010; MROT, and MRO Mapping Orbit (MROM) until May 2011, and two landers (Pathfinder and Viking 1 Lander).

The combination of these multiple data sets provides information on Mars gravity, tides, and orientation. Data from the landers can yield a more precise Mars orientation model including precession, obliquity rate, epoch angles of the Mars pole, and polar motion (Konopliv et al., 2006). Radio tracking data from orbit are more sensitive to gravitational and tidal perturbations of the central body. MRO and ODY are still operating in orbit about Mars, and an additional ~ 4 years of data since MRO110C for each spacecraft are now available on the PDS to help refine those models. Here, we present our work on MGS, ODY and MRO radio tracking data analysis to determine Mars static and time-variable gravity field, and the Love number k_2 . Our solution includes

MGS SPO 1 and 2, GCO, and MAP (<http://pds-geosciences.wustl.edu/missions/mgs/rsraw.html>), ODYT, and ODYM until November 2014 (<http://pds-geosciences.wustl.edu/missions/odyssey/radioscience.html>), and
65 MROT, and MROM until March 2015 (http://pds-geosciences.wustl.edu/mro/mro-m-rss-1-magr-v1/mrors_0xxx/).

The 16 years of radio tracking data cover about 1.5 solar cycles and provide crucial information on the evolution of the seasonal CO₂ cycle (Wood and Paige, 1992). The seasonal mass exchange between the Mars polar caps can be
70 indirectly measured estimating the time-variable zonal gravity coefficients. Any mismodeling of the atmospheric drag, which acts on all of these three spacecraft, but especially on MRO because of its lower altitude, reduces the value of the tracking data, and can especially compromise the seasonal gravity monitoring (Konopliv et al., 2011). For this reason, we have implemented a more accurate
75 upper atmosphere model in our Precise Orbit Determination (POD) program, GEODYN II (Pavlis et al., 2013), to better capture and model the atmospheric density variability (Genova et al., 2015b). The refinement of the atmospheric model leads to more accurate orbits that provide a more stable solution of tides, and static and time-variable gravity field.

80 This paper is structured as follows. In Section 2, we discuss the data included in our gravity solution. In Section 3 and 4 we introduce forces and spacecraft modeling and the estimation method, respectively. Finally, we will show the static gravity field to degree and order 120 in Section 5.1, gravity/topography correlation in Section 5.2, Free-air and Bouguer anomalies that have enabled
85 the determination of the crustal thickness at higher resolution in Section 5.3, tides in Section 5.4 and time-variable gravity zonal harmonics in Section 5.5.

2. Data

We determined the static and time-varying gravity field of Mars by analyzing the radio tracking data of the three NASA orbiters MGS, ODY and MRO. These
90 spacecraft were designed to host radio sub-systems capable of providing X-band

radio links for telemetry and geodetic tracking between the spacecraft and the Deep Space Network (DSN) station complexes. The geodetic measurements of interest for POD consist of *range rate* observables, related to the relative velocity between the station and the probe in the line of sight through the Doppler shift
95 of the signal, and *range* observables, which are the relative distances between the ground station and the spacecraft measured by the round trip propagation time of the radio signal.

Three types of interplanetary radio links are typically differentiated: 1-way when the signal is transmitted directly from the spacecraft to the DSN station;
100 2-way when the signal is transmitted by a DSN station and sent coherently back to the same station by a transponder on the spacecraft; and 3-way similar to 2-way with the only difference being that the transmitting and receiving antennas on Earth (Asmar et al., 2005). The 1-way data must rely solely on the stability of the onboard spacecraft oscillator, instead of the highly-stable
105 oscillators (H₂-master) at the DSN ground stations. MGS was equipped with an Ultra Stable Oscillator (USO) that guaranteed a stability of 10^{-13} , and provided high-quality data at X-Band. Therefore, the MGS 1-way data are included in our solution, and help fill gaps in the 2- and 3-way tracking data coverage in particular (Lemoine et al., 2001). The stability of the ODY and
110 MRO spacecraft oscillators, on the other hand, is one order of magnitude worse than the MGS USO (Mazarico et al., 2007; Konopliv et al., 2011), and, for this reason, these data are excluded from the solution.

The gravity solution depends significantly on the geodetic altitude and latitude coverage of the radio tracking data. Lower orbital altitudes provide better
115 sensitivity to short-wavelength signals and improved gravity resolution. Figure 1 shows the coverage provided by all three Mars orbiters during their mapping and transition phases. The MGS mapping phase, which started on 20 February 1999, was in a frozen sun-synchronous, near-circular, polar orbit with the periapsis altitude at ~ 370 km and the dayside equatorial crossing at ~ 2 PM
120 LST. The lowest altitude data were collected by MGS during the SPO phases 1 and 2 from March to September 1998. In this period, the spacecraft was lo-

cated in a 11.6 h elliptic orbit with the periapsis at 170 km altitude (Lemoine et al., 2001). However, the amount of data collected during this phase was low, because the High Gain Antenna (HGA) was still stowed on the spacecraft bus. During SPO-2 (April–July1998) some limited periapsis data were provided by tracking of the Low Gain Antenna (LGA). After aerobraking, MGS was operated with the HGA pointed continuously to Earth, acquiring data at ~ 400 km for 2 weeks (GCO phase). The HGA was deployed five weeks later to allow collecting radio tracking data with the nadir deck pointed toward Mars.

Mars Odyssey and MRO radio tracking data were also collected at altitudes of ~ 200 km during orbital transition phases that followed aerobraking. On 11 January 2002 nearly continuous ODY radio data were acquired for ~ 4.5 days (ODYT). MRO collected low altitude data from 30 August to 11 September 2006 as shown by the light-blue dashed line (MROT) in Figure 1. ODY and MRO began their mapping phases with the HGA already deployed on 19 February 2002 and 17 November 2006, respectively. ODY is in a near sun-synchronous polar orbit with a periapsis at ~ 390 km altitude and 85°S latitude, and a descending node at 4-5 PM LST. The orbit eccentricity is ~ 0.008 with the apoapsis located in the northern hemisphere at 450 km altitude (Saunders et al., 2004). MRO is in a lower 255×320 km orbit that is also polar and sun-synchronous. The orbit configuration is frozen, similar to Mars Odyssey but with a different fixed crossing time at the ascending node (3 PM), and the periapsis at altitude of 255 km, and latitude of 82°S . The data included in the GMM-3 solution are summarized in Table 1.

Figure 2 shows the level of noise of the whole analyzed 2-way data for MGS (red dots), ODY (green), and MRO (blue) at different tracking geometries. The averaging time of these data is 10 s, and the data fits in Figure 2 are scaled at a 60-s integration time. The horizontal axis in this figure represents the Sun–Earth–Probe (SEP) angle, also called solar elongation angle, which provides information on the radio signal path between the Earth station and the spacecraft. The largest source of error on the radio tracking measurements is the dispersion due to the solar plasma. Low SEP angles indicate that the

Table 1: MGS, Mars Odyssey, and MRO radio tracking data in GMM-3.

	Mission Phase	Dates		Number of Measurements
		From	To	
MGS	SPO-1	27 March 1998	1 May 1998	22189
	SPO-2	28 May 1998	17 Sept. 1998	142206
	GCO	4 Feb. 1999	19 Feb. 1999	51663
	MAP	20 Feb. 1999	4 Jan. 2006	6054461
ODY	ODYT	11 Jan. 2002	15 Jan. 2002	22154
	ODYM	20 Feb. 2002	5 Nov. 2014	8481081
MRO	MROT	30 Aug. 2006	23 Sep. 2006	101915
	MROM	26 Dec. 2006	28 March 2015	8752679

signal passed close to the solar corona, which perturbs the phase/frequency stability of the radio link (e.g. Iess et al. (2014)). A very significant effect at low solar elongations, Doppler and range measurements for $SEP \leq 20^\circ$ have not been included in our solution.

The typical X-band MRO accuracy is ~ 0.05 mm/s at higher SEP that is compatible to the requirements of the onboard radio science instrumentation (Zuber et al., 2007). However, the level of noise for MRO is 20% larger than that of ODY and it is close to that of MGS. MRO range rate noise is inflated from its potential by a periodic signature with a peak at 0.2-0.3 Hz in the frequency domain that began during the safemode on 31 May 2006 (Konopliv et al., 2011; Genova et al., 2015b). We initially processed MRO Doppler data at 1-s samples that exhibited a $\sim 40\%$ higher level of noise with respect to the compressed 10-s data. Averaging these data at a count interval of 10-s enabled us to reduce the effect of that periodic signature as shown in Figure 3. The source of the perturbing signal is related to the radio sub-system electronics since after safe mode entry in March 2014 the switch to the backup transponder alleviated this problem and the level of noise decreased by $\sim 40\%$ for a count interval of 1s (Figure 3). However, the anomaly has not been removed completely and the

quality of the averaged 10-s data has slightly improved as showed in Figure 2 and 3.

3. Forces and spacecraft models

The Precise Orbit Determination (POD) of MGS, ODY, and MRO requires
 175 highly accurate force and spacecraft models. In Section 3.1 we introduce the
 gravitational and tidal fields of Mars, and in Section 3.2 we describe the model-
 ing of the non-conservative forces. Atmospheric drag, solar radiation pressure,
 and Angular Momentum wheel Desaturation (AMD) thrusting are the three ma-
 jor non-conservative perturbations that act on the spacecraft. To reconstruct
 180 a high-fidelity spacecraft trajectory, we need to model the design of the three
 spacecraft including areas, masses, and optical properties of their components
 for the non-conservative perturbations, and the antenna offsets for measurement
 modeling. In Section 3.3 we also show the benefits of the accurate knowledge of
 the antenna offset.

3.1. Gravitational and tidal fields

The gravity field of Mars is modeled as a spherical harmonic expansion
 (Kaula, 2000), as follows:

$$U = \frac{GM}{r} \left\{ 1 + \sum_{l=2}^m \left(\frac{a_e}{r} \right)^l \sum_{m=0}^l [\bar{C}_{lm} \cos m\lambda + \bar{S}_{lm} \sin m\lambda] \bar{P}_{lm}(\sin \phi) \right\} \quad (1)$$

where GM is the product of the gravitational constant and planetary mass, a_e
 = 3396 km is the reference equatorial radius, \bar{P}_{lm} are the normalized associated
 190 Legendre functions of degree l and order m , \bar{C}_{lm} and \bar{S}_{lm} are the normalized
 spherical harmonic coefficients, and r , λ , and ϕ are the body-fixed spherical
 coordinates of radial distance, longitude, and latitude, respectively. The rela-
 tionship between normalized and unnormalized coefficients is:

$$\begin{pmatrix} C_{lm} \\ S_{lm} \end{pmatrix} = \left[\frac{(l-m)!(2l+1)(2-\delta_{0m})}{(l+m)!} \right]^{\frac{1}{2}} \begin{Bmatrix} \bar{C}_{lm} \\ \bar{S}_{lm} \end{Bmatrix} \quad (2)$$

where C_{lm} and S_{lm} are the unnormalized coefficients and δ_{0m} is 1 if $m = 0$, and
 195 is zero otherwise (Kaula, 2000).

The *a priori* gravity field adopted in this study is the MROMGM0032 model up to degree and order 95 (Lemoine, 2009). This field was retrieved using MROT and MROM until August 2008, ODYT and ODYM through 2007, and MGS SPO, GCO, and MAP through the end of 2004. We used the same coordinate
 200 system of the MROMGM0032 model, which is based on a more complete Mars orientation model with nutation recovered by Konopliv et al. (2006) with MGS, Mars Odyssey, Pathfinder, and Viking landers' data sets.

The modeling of the gravity field of Mars also includes the time-varying geopotential that accounts for the redistribution of mass associated with the
 205 CO₂ seasonal cycle. This long-term variation, which is due to the exchange of mass between the atmosphere and the seasonal CO₂ ice caps (Sanchez et al., 2006), is modeled with time-variable low-degree zonal harmonic coefficients. We consider the time-dependent \bar{C}_{20} and \bar{C}_{30} to account for the seasonal evolution of carbon dioxide that condenses and sublimates at the surface of Mars (Karatekin
 210 et al., 2005, 2006; Smith et al., 2009). The CO₂ distribution on the polar caps leads to significant variations of Mars flattening and "pear-shape". The time-dependent function of the gravity harmonic coefficients is given by:

$$\Delta\bar{C}_{lm} = A_{\bar{C}_{lm}}^k \cos\left(\frac{2k\pi}{T}\Delta t\right) + B_{\bar{C}_{lm}}^k \sin\left(\frac{2k\pi}{T}\Delta t\right) \quad (3)$$

where $A_{\bar{C}_{lm}}$ and $B_{\bar{C}_{lm}}$ are the amplitudes of the periodic functions for the coefficient \bar{C}_{lm} , $T = 686.98$ days is the orbital period of Mars, Δt is the elapsed
 215 time with respect to the reference epoch (1 January 2000 00:00:00 UTC), and k is the fractional part of the Martian year. Table 2 shows the time-variable \bar{C}_{20} and \bar{C}_{30} adopted in this study as *a priori* model for annual and semi-annual variability ($k=1,2$).

The *a priori* coefficients of these time-variable coefficients were obtained
 220 by Lemoine et al. (2006), who focused on the estimation of these Mars geophysical parameters and atmospheric density with MGS tracking data. These

Table 2: Time-variable zonal harmonic coefficients of degrees 2 and 3.

	Annual (k=1)		Semi-annual (k=2)	
	A	B	A	B
\bar{C}_{20}	6.2×10^{-10}	-4.3×10^{-10}	1.5×10^{-9}	1.1×10^{-9}
\bar{C}_{30}	2.2×10^{-9}	1.9×10^{-9}	4.1×10^{-10}	3.1×10^{-10}

time-dependent coefficients indeed take into account the cumulative effect of both ice caps and atmosphere. To determine the mass distribution of the polar caps, we need to separate the contribution of Mars atmospheric pressures on the surface of the planet from the time-dependent gravity coefficients. For this reason, we adopted the procedure developed for Earth satellites Boy et al. (2002) that provides the gravity field contribution of global atmospheric pressure loading. Atmospheric pressure variations are one of the sources of surface gravity perturbations. Studies on Earth’s gravity field showed the methodology to obtain the gravity spherical harmonic coefficients from the expansion of input pressure field into a series of spherical harmonics (Boy et al., 1998; Petrov and Boy, 2004; Boy and Chao, 2005). For a thin-layer atmosphere acting on Mars, these coefficients, which represent the atmospheric contribution to the gravity potential into a series of spherical harmonics, are given by:

$$\begin{aligned}
 C_{lm}^a &= \frac{3}{\bar{R}\rho g_0} \frac{1+k_l'}{2l+1} C_{lm}^p \\
 S_{lm}^a &= \frac{3}{\bar{R}\rho g_0} \frac{1+k_l'}{2l+1} S_{lm}^p
 \end{aligned}
 \tag{4}$$

where C_{lm}^p and S_{lm}^p are the spherical harmonic coefficients of the surface pressure field, $\bar{R} = 3389.5$ km is the mean Mars radius, $\rho = 3.933$ kg/m³ is the mean atmospheric density, $g_0 = 3.71$ m/s² is the mean surface gravity, and k_l' is the load Love number of degree l (Boy and Petrov, 2005). The C_{lm}^a and S_{lm}^a coefficients were derived with the surface pressure grids from the Mars-Global Reference Atmospheric Model (Mars-GRAM) 2010 (Justus et al., 1996;

Justus and James, 2001; Justh et al., 2011) with $2.5^\circ \times 2.5^\circ$ spatial and 2-hour time resolution. Those grids were converted into spherical harmonics using the same normalization defined for the gravity coefficients. We compared the Mars-GRAM 2010 surface pressure maps with results of Mars Climate Database (MCD) (Millour et al., 2015) and found they gave consistent results. During the evaluation of the pressure fields, we consider the Mars topography, the solar activity, the re-scaling of the 10.7-cm-wavelength flux at average Earth orbit (1 AU) to Mars position, and the level of dust opacity in background or during dust storms (Smith, 2009). As for the Earth case, the C_{00}^a coefficient is 0 to remove the effect of the mean surface pressure. The 2-h sampling of Mars surface pressure grids allows modeling diurnal and semi-diurnal atmospheric tides. In the case of Earth satellites, the atmospheric tidal signal is removed because they adopt a 6-h sampling that corresponds to the Nyquist frequency of the semidiurnal tide (Boy and Petrov, 2005).

Mars' loading Love numbers k'_l at each degree l are unknown and the lower degrees depend strongly on the Mars interior structure. Sanchez et al. (2006) assumed a rigid Mars with $k'_2 = -0.06$ (Defraigne et al., 2000), and all other k'_l coefficients equal to zero. A more accurate modeling of Mars surface loading was reported in Métivier et al. (2008) computing loading deformations with different models of the interior structure, from a solid core to a liquid core with a radius of 1868 km. Nevertheless, the k'_1 is independent from the interior model and is equal to -1. We ran different cases with and without the C_{lm}^a and S_{lm}^a coefficients showing that MGS, ODY, and MRO radio tracking data are sensitive to the atmospheric contribution. However, we have not noticed significant discrepancies between solutions with different loading Love numbers. For this reason, we present only the gravity solution determined with C_{lm}^a and S_{lm}^a coefficients computed assuming a liquid core radius of ~ 1500 km.

We also need to account for the tidal effects that Phobos and the Sun exert on Mars. The tidal perturbation of Deimos is negligible. The second-degree tidal potential acting on a spacecraft is given by:

$$U = k_2 \frac{GM_p}{R} \frac{R^6}{r^3 r_p^3 \left[\frac{3}{2} (\hat{r} \cdot \hat{r}_p)^2 - \frac{1}{2} \right]} \quad (5)$$

where \hat{r} and \hat{r}_p are the relative positions of the central and perturbing bodies, respectively, k_2 is the Love number of the second degree, M_p is the mass of the perturbing body (e.g., Sun and Phobos), and R is the equatorial radius of the central body. We modeled the degree 2 tidal perturbation with order-dependent k_{2m} , which produce time dependent changes in the gravity field coefficients C_{2m} and S_{2m} (McCarthy and Petit, 2004). However, these Love numbers are expected to be equal, so we assumed as *a priori* $k_{20}=k_{21}=k_{22}=0.17645$ (Konopliv et al., 2011). These three Love numbers are represented in this expanded tidal model with real and imaginary parts. The latter reflects the phase lag (γ) in the deformation response of Mars to tidal forces. The k_{20} coefficient has to be real since there is no phase lag on \bar{C}_{20} . The $\text{Im}(k_{21})$ and $\text{Im}(k_{22})$ provide information on the dissipation of the mantle. Previous studies determined the tidal phase angle by measuring the secular acceleration of Phobos that is in a nearly circular orbit. Previous studies reported γ values ranging between 0.6° and 0.7° (Bills et al., 2005; Rainey and Aharonson, 2006; Lainey et al., 2007; Jacobson, 2010). However, we assumed a zero *a priori* $\text{Im}(k_{21})$ and $\text{Im}(k_{22})$. The positions of Mars, Phobos and Deimos, are obtained from the JPL ephemerides DE421 (Folkner et al., 2008) and MAR085 (Jacobson, 2010) and are required for third-body perturbations and Doppler and range processing.

3.2. Non-conservative forces

The orbits of spacecraft about Mars are perturbed by substantial non-conservative forces, such as atmospheric drag and solar and planetary radiation pressures. The magnitude of these perturbing forces is related to the orbital geometry of these spacecraft. Atmospheric drag is indeed the largest perturbation acting on MRO because of its low-periapsis orbit, whereas solar radiation pressure is the largest one on the higher altitude MGS and ODY spacecraft. Therefore, the modeling of all the non-conservative forces acting on each spacecraft must be accurate.

The atmospheric drag acceleration is modeled as follows:

$$a_{drag} = \frac{1}{2} \frac{\rho C_D V^2}{m} \sum_i A_i \mathbf{n}_i \cdot \mathbf{n}_V \quad (6)$$

where V and \mathbf{n}_V are the spacecraft velocity module and direction, and m and C_D are the spacecraft mass and a scale factor of the drag acceleration. All three spacecraft are treated as a combination of flat panels that reproduce the box shape of the spacecraft bus, the solar arrays, and the HGA. The latter components are modeled as moveable plates. The parameters A_i and \mathbf{n}_i are the surface area and normal vector for each of the macro model plates. We modeled the interplate self-shadowing of the spacecraft physical model for ODY and MRO in the computation of the cross-sectional areas for the atmospheric drag and radiation pressure (Mazarico et al., 2009). Shadowing on MGS is minimal (Konopliv et al., 2011). The aerodynamic expression of the drag takes into account only along-track effects neglecting lateral wind and aerodynamic lift. We implemented the Drag Temperature Model - Mars (DTM-Mars) (Bruinsma and Lemoine, 2002) in GEODYN II to provide predictions of atmospheric total density (ρ). The DTM-Mars model is based on the assumption of independent diffusive equilibrium of different atmospheric constituents (CO_2 , CO , O_2 , O , N_2 , Ar, CO , He, H_2 , and H) and computes the total atmospheric density as the sum of the partial density of each species with respect to position (altitude, latitude, and local solar time), solar activity, and season. Genova et al. (2015b) described the model in detail and used the methodology to recover the long-term periodicities of the atmospheric constituents with radio tracking data. The *a priori* atmospheric model is based on the results of Bruinsma and Lemoine (2002). Future study will be dedicated retrieving simultaneously the Mars gravity field and DTM-Mars atmospheric density variabilities (Genova et al., 2015b).

To further mitigate atmospheric mismodeling, we adjusted one atmospheric drag coefficient (C_D) for each spacecraft orbit (~ 1.95 h MGS, ~ 1.95 h ODY, ~ 1.87 h MRO), with only a very loose *a priori* uncertainty (equal to 10, Genova et al., 2015b). These coefficients are time-correlated within each POD arc (~ 3 -

5 days) with a time-correlation length of one orbital period (Rowlands et al., 2010; Lemoine et al., 2013), which acts to smooth the C_D time series and prevent unreasonable values in periods with no tracking. If an estimated C_D , also
330 called the ballistic coefficient, is not close to predictions from the spacecraft design (Gaposchkin and Coster, 1988), this is a strong indication that it compensates for an increase or decrease in the atmospheric density not captured by the numerical atmospheric model. In particular, dust storms, which are not
335 modeled in our version of the DTM-Mars, lead to enhanced atmospheric densities. Therefore, a high correlation between estimated C_D and dust opacity in the atmosphere is a good indicator of the quality of the atmospheric recovery with our DTM-Mars/ C_D approach (Genova et al., 2015a). The range of possible ballistic coefficients for the expected atmospheric densities in the along-track direction is $\sim 1.7 - 2.1$ for MGS (Tolson et al., 1999), $\sim 1.8 - 2.2$ for ODY (Tolson
340 et al., 2005), and $\sim 1.7 - 2.3$ for MRO (Tolson et al., 2008). Nevertheless, the spacecraft C_D cannot be known to better than $\sim 4\%$ (Gaposchkin and Coster, 1986).

In addition, accurate modeling of non-conservative forces requires precise knowledge of spacecraft masses, which are reported in the Maneuver Performance Data (MPD) files on PDS (MGS at <http://pds-geosciences.wustl.edu/missions/mgs/rsraw.html>, ODY at <http://pds-geosciences.wustl.edu/missions/odyssey/radioscience.html>, and MRO at http://pds-geosciences.wustl.edu/mro/mro-m-rss-1-magr-v1/mrors_0xxx/), spacecraft shape, and attitude (MGS at http://naif.jpl.nasa.gov/pub/naif/pds/data/mgs-m-spice-6-v1.0/mgsp_1000/data/ck/, ODY at http://naif.jpl.nasa.gov/pub/naif/pds/data/ody-m-spice-6-v1.0/odsp_1000/data/ck/, and MRO at http://naif.jpl.nasa.gov/pub/naif/pds/data/mro-m-spice-6-v1.0/mrosp_1000/data/ck/). The spacecraft bus follows the attitude of the spacecraft reference frame, and solar arrays and HGA have independent orientations to allow illuminating the solar panels and pointing the high gain antenna towards Earth. The
355 modeling of solar, albedo, and thermal radiation pressure must account for the material properties of each spacecraft surface. The specular and diffusive coeffi-

cients for each plate are based upon the combination of surface type (You et al., 2007). The radiation pressure scale factor (C_R) is fixed to 1 and not adjusted
360 in our solution. Instead, we estimate a set of empirical along- and cross-track
once-per-revolution (OPR) periodic accelerations to absorb errors in the radiation
pressure model. The *a priori* uncertainty of the along- and cross-track
OPR accelerations assumed in this analysis were 1×10^{-6} and 1×10^{-9} m s⁻²,
365 respectively. A possible mismodeling of the solar radiation pressure exists due
to the contribution of the atmospheric dust. The increase of the level of dust
in the Martian atmosphere significantly reduces the solar flux as a spacecraft
passes near the limb of Mars. Only Mars Odyssey experiences these grazing oc-
cultations, and we refined the modeling of Mars' umbra and penumbra, which
is used in GEODYN II, by increasing the radius of Mars ellipsoid during these
370 events. Several incremental altitudes between 5 and 100 km were tested, and
we selected the altitude of ~ 40 km since it provided lower OPR cross-track
accelerations. The effect of grazing occultations on MGS and MRO is negligible
(Konopliv et al., 2011).

The attitude control of MGS, ODY, and MRO relies on reaction wheels.
375 The large torques that act on each spacecraft lead to the saturation of the mo-
mentum wheels, and therefore, coupled pairs of thrusters are used periodically
to desaturate the wheels, during Angular Momentum Desaturation (AMD) ma-
neuvres. Though designed to produce no net acceleration, small imbalances
typically yield residual ΔV s, which are an important perturbation on the orbit
380 of the spacecraft. Since the MRO AMDs occurred every day for the first month
of the mission, and every 2-4 days afterwards, we arranged the start and stop
times of the MRO POD arcs around these maneuvers to avoid their adverse
effects. The Mars Odyssey and MGS AMDs occurred much more frequently
(once or twice per day) and cannot be avoided because very short arcs would
385 be detrimental to gravity recovery. We instead estimated one impulsive burn at
the midpoint of the MGS AMD duration span to compensate for AMD-induced
accelerations on the spacecraft. We adopted a different approach for ODY, be-
cause two thruster pairs were used during AMD events, in general 10 min per

pair. For this reason, we estimated two impulsive burns at the start and the
390 end times of the maneuvers to compensate for different thruster magnitudes and
directions.

3.3. Spacecraft Antenna Offsets

The accurate analysis of radio tracking data requires a precise definition
of the center of integration for the spacecraft trajectory, which generally is its
395 center-of-mass (CoM). The relative distance between this point and the antenna
phase center has to be known accurately in order to compute the predicted
observables without systematic errors. For example, an unknown displacement
of the spacecraft center-of-mass may be artificially interpreted as an apparent
acceleration from the Doppler measurements, which can significantly harm the
400 gravity field recovery and orbit determination.

We accounted for the antenna offsets for MGS, ODY, and MRO based on
their spacecraft center-of-mass. We updated MGS, ODY, and MRO center-of-
mass positions after every Orbit Correction Maneuvers, to account for propellant
consumption. However, the offsets of the MRO HGA require more precise mod-
405 eling since its large solar arrays can gimbal rapidly and significantly displace the
center-of-mass. The solar arrays, in particular, but also the HGA, can displace
the MRO CoM by ~ 20 cm, and such a mismodeling can lead to erroneous ap-
parent range rates greater than 1 mm/s. Therefore, we computed the position
of MRO's center-of-mass every second using the masses and telemetered orien-
410 tation of the moveable spacecraft components (solar arrays and HGA). Figure 4
shows MRO Doppler residuals during a single tracking pass obtained with (red
dots) and without (black dots) the 1-s time-variable corrections of the center-
of-mass position. The uncorrected range-rate series clearly shows two erroneous
signals that correspond to the rapid movement of the center-of-mass (blue line).
415 These rapid CoM displacements are due to the re-orientation of MRO solar ar-
rays before and after the transition into eclipse of the spacecraft. These events
can occur every orbit, so the high-rate CoM computation is necessary to avoid
large anomalous Doppler residuals signatures that can compromise the results

obtained with MRO data.

420 **4. Method**

We processed MGS, ODY, and MRO radio tracking data dynamically over a continuous span of time using the NASA GSFC GEODYN II Orbit Determination and Geodetic Parameter Estimation Program (Pavlis et al., 2013). The methodology of GEODYN II to process range and range-rate data is through
425 a batch least-squares scheme that combines all observations within one time period (*arc*) in order to estimate a selected set of parameters (Tapley et al., 2004). The least-squares technique consists of an adjustment of the estimated parameters to minimize the discrepancies between the computed observables and actual measurements (*residuals*). The residuals contain information on all
430 sources of mismodeling (*e.g.*, atmospheric density, gravity field). We distinguish arc parameters (*local*) that affect only measurements within one arc (*e.g.*, spacecraft initial state) and common parameters (*global*) that affect all measurements (*e.g.*, gravity field coefficients).

We adopted arc lengths between 2.5 and 8 days depending on the spacecraft
435 and mission phase. The typical arc length during the mapping phase of these missions is ~ 5 days for MGS and ODY, and ~ 2.5 days for MRO. The Doppler data were processed by weighting each arc with the RMS of the residuals. In each arc, we estimated the spacecraft initial state (position and velocity), one drag scale coefficient per orbit (using time-correlation constraint), and along- and
440 cross-track cosine and sine OPR empirical accelerations in a batch least-squares filter. We do not adjust either radiation pressure scale factors or spacecraft panel reflectivities. OPR accelerations absorb orbit perturbations due to solar, and planetary radiation pressure and short timescale drag effects (*e.g.*, local solar time variations of the atmospheric density). Furthermore, time-correlated
445 drag scale coefficients mitigate mismodeling of the long-term variability (annual and semi-annual) of Mars atmospheric density provided by DTM-Mars.

After data convergence of one arc through iterative batch least-squares to

estimate the arc parameters, we generate a set of partial derivatives for both arc and common parameters, and transform these into a normal equation (Tappley et al., 2004). Then, all the individual arcs' normal equation systems are combined and inverted, yielding the final estimates of the common parameters. Arc parameters can be solved simultaneously, or they can be solved implicitly by taking into account their Schur complement (Demmel, 1997). In Section 5 we present the results and formal uncertainties of the static and time-variable gravity field, and tides. We recommend a calibration factor of 3 for the uncertainties to obtain conservative error estimates for the gravity field coefficients and Love number, k_2 . Mission by mission analysis and solutions with different estimation strategies showed variations of the estimated parameters within 3σ .

5. Mars static and time-variable gravity field, and tides

5.1. Static gravity field

We present our static gravity field of Mars in spherical harmonics to degree and order 120, named **Goddard Mars Model 3 (GMM-3)**, which can be available from the Geosciences Node of PDS http://pds-geosciences.wustl.edu/mro/mro-m-rss-5-sdp-v1/mrors_1xxx/. This model follows previous solutions derived at NASA GSFC: GMM-1 and GMM-2 that employed S-band tracking data from Mariner 9 and Viking 1-2 spacecraft (Smith et al., 1993; Lemoine et al., 1994), and GMM-2b was developed using MGS radio tracking data and altimeter crossovers until February 2000 (Lemoine et al., 2001). The latest GSFC model, MROMGM0032 to degree and order 95, included MRO and ODY data until 2008, and the complete MGS data set (Lemoine, 2009). In comparison, the most recent gravity solution released on NASA's PDS is the 110x110 field MRO110C, which was derived at JPL by Konopliv (2012) from 5 years of MRO data (2006-2011), 6 years of ODY data (2002-2008), and the entire set of MGS data.

Figure 5 shows the root-mean-square (RMS) power spectra for the Mars gravity solutions GMM-3, MRO110C, and MROMGM0032, as well as their

associated formal uncertainties. The RMS power of the coefficients and relative standard deviations are computed following Kaula (2000). The improved error estimates are due to the impact of MRO and ODY latest data. Although the
480 orbits of these two spacecraft have not been changed, the new data allow a better longitudinal coverage of the planet, especially, in the equatorial region. Furthermore, the MRO data after April 2014 are of higher quality than previous data, thanks to the switch to the second, redundant transponder (an operational change made after a safe mode).

485 We obtained the GMM-3 model with a Kaula power law constraint of $15 \times 10^{-5}/l^2$, only applied at degrees l greater than 90. Figure 5 shows that the unconstrained solution (magenta line) begins to deviate from a smooth power law around degree 90-95, therefore implying a global resolution of ~ 115 km at the surface. Nevertheless, the resolution can vary significantly, especially with latitude since the periapses of all spacecraft orbits have been located in the southern
490 hemisphere. For this reason, we adopted the degree strength approach that was illustrated by Konopliv et al. (1999), Konopliv et al. (2013), and Mazarico et al. (2014) to determine the local resolution on a global scale for Venus, the Moon, and Mercury, respectively. This method is based on the comparison between
495 the expected gravity accelerations, approximately $8.5 \times 10^{-5}/l^2$, and the localized formal uncertainties computed at each degree. The degree at which the expected value and the error intersect corresponds to the maximum resolution at that location on the globe. We used the GMM-3 covariance matrix to map the degree strength, as shown in Figure 6. The minimum resolution is ~ 84 in
500 a region close to Arcadia Planitia. The south polar region shows a resolution slightly better than degree 100. To compute gravity accelerations and errors we accounted for a spherical shape of Mars to avoid oversampling at the poles that can lead to unlikely resolutions.

Figure 6 also shows the free-air gravity anomalies when expanded only up to
505 the local degree strength at each location. This representation of gravity anomalies can enhance the geophysical interpretation of specific features detected on the surface. The signal to noise ratio in the higher harmonics can jeopardize the

geophysical interpretation, by introducing artifacts that can lead to misleading results. Therefore, in Section 5.2 we discuss the correlation of gravity and topography, by comparing free-air gravity anomalies that follow from the degree strength solution, and the MOLA topography (Smith et al., 1999b).

5.2. Global and localized gravity/topography correlation

Short-wavelength free-air gravity anomalies are driven by the widespread occurrence of isostasy from topography. Therefore, high correlations between gravity and topography harmonic expansions at higher degrees have typically been considered as indicators that the gravity solution is well determined. On the other hand, gravity anomalies characterized by longer wavelength (lower degrees) are probably due to the finite strength of the mantle or density differences associated with convective flow in the mantle (Jeffreys, 1959; Runcorn, 1965; Watts and Daly, 1981), and they do not correlate well with topography.

Figure 7 shows the correlation of the gravity anomaly predicted by MOLA surface topography with three gravity field solutions: GMM-3, MRO110C, and GMM-3b (which was derived with the same methodology as GMM-3, but with a limited dataset identical to that used by Konopliv (2012)). This plot is focused on the range of degrees between 50 and 110, where high correlation with topography is expected. The GMM-3b solution is better correlated with gravity from topography (computed with Wieczorek and Phillips (1998) technique) compared to MRO110C, and between degrees 70 and 85 its correlation is closer to ~ 0.9 . The GMM-3 solution shows further improvement in correlation, up to degree 100. These results demonstrate that the improvements in the GMM-3 model are primarily due to the refinements of the force and spacecraft modeling. The DTM-Mars atmospheric model, in particular, provides more accurate density profiles that allowed us to improve the modeling of atmospheric drag (Genova et al., 2015b). However, the differences between GMM-3 and GMM-3b show that the data still being acquired by ODY and MRO in particular continue to contribute useful information for the determination of Mars' static gravity field.

We also computed the admittance and correlation between GMM-3 and to-

pography (**Figure S1**) to examine how the lithosphere responds to topographic loads of different wavelengths. The admittance has a rather flat trend between
540 degrees 30 and 90 with a large amplitude of ~ 105 mGal km $^{-1}$ that would be expected for uncompensated topography (Wieczorek, 2007). The topography of Mars is characterized roughly by two distinct age zones, where older regions are isostatically compensated at relatively shallow depth, and geologically younger regions are only partially compensated (Phillips and Saunders, 1975;
545 Zuber et al., 2000). For this reason, a local region analysis is necessary for a better understanding of the crust and mantle interior structure.

Figure 8 shows the MOLA topography compared to the free-air gravity anomalies of the GMM-3 degree strength solution for the north and south polar regions. The highlands in the south are highly correlated with the gravity
550 anomalies. MGS, ODY, and MRO have their orbital periapses at those latitudes, so the resolution of the gravity field can be expected to be higher, at ~ 100 km. Topographic features of this size are detectable in the free-air anomaly map, such as negative anomalies at craters Phillips and Schmidt in the Mare Australe quadrangle. To investigate the local gravity/topography correlation over
555 the polar caps, we used a cap of 30° directly centered on the north and south poles with one taper concentration factor of 0.9999, resulting in a windowing function with $L_{win} = 13$ (Wieczorek and Simons, 2005). **Figure S2** shows local correlations and admittances for both poles. The south pole has higher gravity/topography correlation and lower admittance, suggesting a higher level of
560 compensation. The north polar layered terrains are surrounded by lowlands that do not correlate with the positive and negative free-air anomalies (Figure 8). Previous gravity solutions already exhibited this lack of gravity/topography correlation (Zuber et al., 2000; Konopliv et al., 2011), and GMM-3 confirms these results with a sharper definition of those anomalies. The positive gravity
565 anomalies in the north may be due to heterogeneous material in the lower crust or upper mantle, or mascons of sedimentary and/or volcanic deposition in ancient buried impact basins (Phillips et al., 1999; Zuber et al., 2000; Fishbaugh and Head, 2001).

The other unsolved enigma in the northern lowlands is the gravity trough
570 between Acidalia Planitia and Tempe Terra ($\sim 305^\circ\text{E}$ in Figure 9). Zuber et al.
(2000) interpreted that anomaly as a system of buried channels that delivered
water and sediments from Mars' southern highlands into the northern lowlands
before the cessation of resurfacing. That gravity field measured by MGS showed
a gravity trough that extends from Kasei Valles ($25^\circ\text{N}, 310^\circ\text{E}$), a major outflow
575 channel, up to $\sim 75^\circ\text{N}$. The GMM-3 higher resolution provides a better under-
standing of these features that were at the edge of the resolution of previous
gravity solutions. Figure 9 shows the GMM-3 gravity anomalies in that region
of Mars' northern hemisphere. Our higher-resolution gravity field reveals that
this negative anomaly starts at Shalbatana Vallis ($7^\circ\text{N}, 318^\circ\text{E}$), a minor outflow
580 channel, and follows the dichotomy boundary along Xanthe Terra northward by
connecting to Kasei Valles. The western edge of the trough closely follows a
 -1.8 km topographic contour of the highland-lowland dichotomy boundary ex-
tending from Coprates Chasma northward to 55°N . The eastern continuation
of the trough likewise follows a contour that slopes downward to -2.8 km as it
585 continues in a northeasterly direction over Arabia Terra. This system of gravity
troughs is unlikely to be due to buried channels only, since it is elevated with
respect to the Acidalia plains and runs perpendicular to the local topographic
gradient. The topography reveals only drainage features running across the
trough. Thus the free-air anomaly trough is more closely associated with the
590 hemispheric dichotomy boundary itself than with outflow channels.

The anomaly may represent a density contrast in the crust or mantle, per-
haps due to the burial of a flexural moat and a low-density crustal root that
flanks the topographic dichotomy from Xanthe Terra to Tempe Terra. The neg-
ative anomaly of the Thaumasia Highlands represents an analogue case that
595 Williams et al. (2008) interpreted indeed as a consequence of lithospheric flex-
ure from the topography (Figure 2 in Williams et al. (2008)). The highlands
load on the Mars surface would have deflected the lithosphere, leading to the
formation of moats. In the case of the Chryse Planitia, water and sedimentary
material from Shalbatana Vallis and Kasei Valles would have flowed into the

600 moat northward (Tanaka et al., 2003). Furthermore, we compared profiles of
the free-air gravity anomalies and the topographic-based gravity in this region
(including the corrections for finite-scale topography, Wieczorek and Phillips,
1998). **Figure S3** shows these profiles at two latitudes over the edge of Tempe
Terra. Dombard et al. (2004) showed good correlation between free-air gravity
605 anomalies, based on GMM-2b, and topographic-based gravity at those latitudes
suggesting that the gravity trough is related to the sharp topographic bound-
ary. However, our observed and topography-based gravity are not consistent
with this interpretation.

The comparison of gravity and topography provides information on the elas-
610 tic thickness (T_e) in several areas of Mars. We focus on volcanic regions showing
high admittance and good correlation between gravity and topography, to help
understand the lithospheric loading at a finer scale. Figure 10 shows the free-air
gravity anomalies (left panels) and admittance-correlation between gravity and
topography (right panels) for the two main Martian volcanos, Olympus Mons
615 (19°N, 226°E) and Elysium Mons (19°N, 226°E). For admittance and corre-
lation computation, we performed localization using a cap of 30° centered on
each volcano with a windowing function with $L_{win} = 13$ that resulted from
one taper concentration factor of 0.9999 (Wieczorek and Simons, 2005). These
results are generally consistent with previous work (McKenzie et al., 2002; Mc-
620 Govern et al., 2002; Belleguic et al., 2005), but improve the resolution of both
admittance and correlation. However, we note that our admittances and corre-
lations show some differences at the higher degrees with respect to the results
in Konopliv et al. (2011) Figure 14. These discrepancies are in part due to the
different localized spectral analysis adopted by Konopliv et al. (2011), which
625 was based on the spatio-spectral localization method of Simons et al. (1997).
The correlation at Olympus Mons is between 0.9 and 1 up to degree 90, which is
close to the gravity degree strength at those Martian latitudes. The admittance
shows two peaks of ~ 200 mGal/km and ~ 170 mGal/km at degrees ~ 55 and
 ~ 85 , respectively. The average value of the admittance is ~ 140 mGal/km that
630 is consistent with lithospheric flexure in response to surface loading T_e larger

than 150 km (McGovern et al., 2002). Elysium Mons displays a flatter admittance spectrum than Olympus Mons with a mean value slightly lower (~ 130 mGal/km). Its correlation with topography is ~ 0.95 for all degrees between 13 and 95.

635 The vicinity of the Hellas basin represents another volcanic region that was defined by Williams et al. (2009) as the Circum-Hellas Volcanic Province. The volcanoes around the basin are shield-like edifices or caldera-like depressions surrounded by ridged plains. The gravity anomalies in this region are fundamental to defining the mechanisms of formation that generate these volcanic structures. Figure 11 shows the free-air degree strength gravity anomalies over Hellas and its surroundings. Large positive anomalies are present at Tyrrhena (21.39°S, 106.63°E), Hadriaca (30.2°S, 92.79°E), and Amphitrites Paterae (58.7°S, 60.87°E) that may be indicative of dense magma bodies underneath the surface (Williams et al., 2009). On the other hand, volcanos, such as Peneus (57.82°S, 52.65°E), Malea (63.54°S, 51.59°E), and Pityusa Paterae 640 (66.88°S, 36.86°E) that are large caldera-like depressions (Figure 11) show weak gravity anomalies confirming that they may have been the source regions for large quantities of lava flows and/or pyroclastic deposits (Werner, 2009; Sigurdsson et al., 2015).

650 5.3. Bouguer gravity and Crustal Thickness

Following previous work (Zuber et al., 2000), we adopt for Bouguer reduction a bulk density of 2900 kg m^{-3} for the crust. The gravity predicted from topography with this density, calculated using the finite-amplitude expansion of Wieczorek and Phillips (1998) is subtracted from GMM-3 to obtain the Bouguer anomaly potential coefficients. The spherical harmonic coefficients are then expanded. Much of the Bouguer anomaly arises from the hemispheric dichotomy and the polar flattening. These degree-1 and -2 coefficients are removed to reveal local variations in crustal thickness and/or density, neglecting possible long-wavelength signals arising from the mantle and core. The remaining spherical harmonic coefficients are expanded up to degree 90 (resolution of 120 km), 660

avoiding possible aliasing at the highest degrees, as shown in Figure 12. The majority of the signal produced by topography is removed, however the Tharsis volcanos, the giant basins and the Melas Chasma portion of Valles Marineris at 285°E longitude exhibit substantial positive Bouguer anomalies, requiring either
665 denser near-surface crustal material and/or a shallower interface between crust and mantle. In other regions, for example the adjacent areas Ius Chasma to the west, Ophir Chasma to the north, and Coprates Chasma to the east (Figure 9), the gravitational signal of topography is muted, justifying our average crustal density assumption and the accuracy of the GMM-3.

670 We assume a density of 3500 kg m^{-3} for the mantle and perform a non-linear inversion for relief on the crust-mantle boundary, applying a smoothness constraint (Wieczorek and Phillips, 1998) to suppress spurious relief resulting from downward continuation of noise. While the degree strength of GMM-3 exceeds 80 nearly everywhere, the constraint applied reduces the amplitude by
675 0.5 at degree 80 and 0.25 at degree 100, and more appropriate filters might be employed in regions of higher quality. The constraint that the crustal thickness be non-negative results in a minimum average depth of the mantle, equivalent to an average thickness of 42 km. Such a result depends strongly on the density assumptions, producing somewhat more relief if the crust is stratified or
680 the mantle portion of the lithosphere is less dense than we have assumed. The constraint is tightest at the Isidis basin, where substantial volcanic resurfacing with a high density could give the appearance of thinner crust. Given these caveats, we estimate uncertainty in mean crustal thickness to range from 35-50 km, consistent with earlier estimates (Neumann et al., 2004; Wieczorek and
685 Zuber, 2004).

Figure 9c shows the regional Bouguer anomaly in the western hemisphere. Melas and Candor Chasma are distinguished by a positive anomaly over the deepest portion of the Valles Marineris. We interpret the crustal structure in Figure 9d as thinning associated with the rifting (Yin, 2012) that produced
690 Valles Marineris, providing further constraints on the polygenetic origin of the linked system of canyons. Similarly the 2500-km Echus Chasma - Kasei Valles

outflow system is associated with crustal thinning.

The striking association of the dichotomy boundary with the gravity troughs is now resolved. The region of thickened highland crust extends beyond the
695 topographic contour bounding the troughs of low free-air gravity and underlies the troughs. This contour is however tilted by ~ 0.02 degrees in an east-west direction away from the Tharsis bulge (Phillips et al., 2001) and suggests a pre-Tharsis-emplacment equipotential surface. The elevated highland topography was compensated by thicker crust at a point in time when the lithosphere did
700 not support loads; as the lithosphere subsequently thickened it was able to maintain the pre-existing topographic scarp. Tharsis volcanism gave rise to a flexural deformation of the entire region illustrated here, as well, produced substantial changes in climate resulting in outflow channels and erosion. Some of this surficial activity could have distributed crust from the steepest portions
705 of the boundary and distributed it over the Chryse and Acidalia plains, leaving a mass deficit revealed by the free-air gravity troughs. This redistribution of crust then provides an explanation of the association of the dichotomy boundary with the gravity troughs, as an alternative to that of Dombard et al. (2004) or Williams et al. (2008).

710 5.4. Tides

The combined analysis of MGS, ODY and MRO radio tracking data provides further information on the interior structure of Mars. The estimation of the Love number k_2 helps constrain the size of the fluid core of the planet. The Mars k_2 solar and Phobos tide obtained from the global solution is:

$$k_2 = 0.1697 \pm 0.0009 \quad (7)$$

715 and indicates an outer liquid core (Yoder et al., 2003). This value does not need to be corrected for atmospheric tides because we provided separately the gravity contribution of the atmosphere, in which the atmospheric tides are included. The single-spacecraft solutions (MGS, ODY, or MRO) yielded k_2 values from 0.169 to 0.172.

720 The combined estimation of the Love number k_2 is consistent with the MGS
estimation reported in Konopliv et al. (2011). The interpretation of our es-
timated Love number k_2 in interior structure models requires an additional
correction related to the solid tidal friction. The tidal phase lag $\delta_2 \sim 0.5^\circ\text{-}0.6^\circ$
was determined in previous studies by measuring the tidal change in Phobos’
725 orbit (Bills et al., 2005; Jacobson, 2010). Therefore, our measured k_2 must be
scaled by $1/\cos(\delta_2)$. However, this correction is $\sim 6 - 9 \times 10^{-6}$, which is lower
than the k_2 formal uncertainty.

This weak effect of the phase lag on the tides is not currently detectable from
the analysis of MGS, ODY and MRO radio science data. In our solution we tried
730 to estimate separately the real and imaginary parts of the Love numbers k_{20} ,
 k_{21} , and k_{22} . The latter parameter determines the larger perturbation on those
spacecraft orbits causing a secular rate of the orbit inclination. Therefore, the
 k_{20} and k_{21} are not well determined showing ~ 20 and ~ 5 times larger formal
uncertainties than k_{22} , respectively. Furthermore, the results of the $\text{Im}(k_{21})$
735 and $\text{Im}(k_{22})$ lead to unrealistically large phase lags δ_{21} and δ_{22} . Therefore, we
constrained k_{20} , k_{21} , and k_{22} to be the same value (k_2) and we estimated the
 $\text{Im}(k_{22})$ only. Nevertheless, the recovered phase lag is $\delta_{22} = 10^\circ \pm 5^\circ$ and it affects
the k_2 estimation leading to lower values (0.14-0.15). The $\text{Im}(k_{22})$ solutions
depend on which time-variable gravity coefficients are estimated in the global
740 iteration. For this reason, the solution of the static and time-variable gravity,
and the Love number k_2 presented in this work does not include the estimation
of the tidal phase lag.

5.5. Time-variable gravity

The ~ 16 years of continuous Mars data at different altitudes and LST are an
745 unprecedented opportunity to detect the seasonal variation of long-wavelength
gravity coefficients. The seasonal mass exchange between the Mars polar caps
is best observed in time-variable terms of the gravity zonal harmonics, and the
odd-degree zonal amplitudes are $\sim 20\%$ larger than the even-degree’s (Sanchez
et al., 2006; Konopliv et al., 2011). For this reason, previous work focused

750 especially on the determination of the odd zonal, normalized gravity coefficient C_{30} (Yoder et al., 2003; Konopliv et al., 2011; Smith et al., 2009), which provides crucial information on the CO_2 mass exchange between the north and south polar caps.

However, mismodeling of the spacecraft AMDs and the atmospheric drag
755 may compromise the estimation of the time-variations of the gravity field harmonics. Konopliv et al. (2011) showed the effects of errors in MGS and ODY AMDs on the time-varying C_{20} and C_{30} . Furthermore, they also stated that MRO was not expected to help determine the seasonal gravity coefficients since large errors in the atmospheric drag modeling reduce the benefits of those lower-
760 altitude data. The refinement of the atmospheric model in GEODYN II helped us mitigate the MRO orbital errors due to the atmospheric drag (Genova et al., 2015b), and we now find the MRO radio tracking data can be used to extend the seasonal gravity monitoring begun with MGS in 1997 and continued by ODY.

We adopted two different methods to recover the time-variable gravity. The
765 first approach consists of a global inversion of the static gravity field, the Love number k_2 , and of coefficients describing the periodic time dependence of the gravity harmonic coefficients ($A_{\bar{C}_{lm}}^k$ and $B_{\bar{C}_{lm}}^k$, Eq. 3) with the complete MGS, ODY and MRO datasets. The static gravity solution presented in Section 5.1 and the Love number k_2 were retrieved using this approach. The other method is
770 based on a mission by mission analysis creating short batches of one month, from which we estimate separate C_{20} and C_{30} . This strategy has been successfully used to determine variations of the Earth low-degree field from 1976 to 2014 (e.g. Cheng et al., 2013; Lemoine et al., 2014). Both analyses directly inform inter-annual exchanges of ice mass in the polar caps, because we separately account
775 for the gravity contribution of the atmosphere with series of spherical harmonics computed every 2 h from Mars-GRAM2010 input pressure field (Section 3.1).

We first derived the time-variable coefficients $A_{\bar{C}_{lm}}^k$ and $B_{\bar{C}_{lm}}^k$ of the gravity zonal harmonics C_{20} , C_{30} , C_{40} , and C_{50} globally using MGS, ODY and MRO tracking data (Table 3). We have adjusted triple-frequency coefficients for each
780 zonal to measure its annual, semi-annual, and tri-annual mass variations in the

polar caps. Figure 13 shows the inter-annual variability of the retrieved even and odd zonal harmonics during the Martian seasons. The three spacecraft orbits have been perturbed mainly by C_{30} . The effect of the even harmonics on these polar near circular orbits is small. C_{20} and C_{40} lead to secular changes
785 in the longitude of the ascending node, but this precession rate scales with the orbit eccentricity and the cosine of the orbit inclination (Konopliv et al., 2006), which are both close to zero. The seasonal C_{30} affects the argument of periapsis, which provides a stronger signal in the tracking data.

To assess the quality of these results, we computed the correlations between
790 the amplitudes of the time-variable C_{20} , C_{30} , C_{40} and C_{50} and the Love number k_2 as shown in **Table S1**. The correlations between time-variable gravity coefficients and k_2 are negligible, and correlations between even zonal harmonics are very low as well. On the other hand, C_{30} and C_{50} have a good anti-correlation for the semi-annual and tri-annual periodicities, which is ~-0.6 and ~-0.7 ,
795 respectively. However, C_{30} and C_{50} are not strongly correlated and we were able to separate their effects especially for the annual term that shows a small correlation of ~-0.4 .

The global estimation of C_{30} time-variable coefficients is in good agreement with previous gravity solutions (Yoder et al., 2003; Konopliv et al., 2006; Smith
800 et al., 2009; Konopliv et al., 2011), which were derived with ODY and/or MGS tracking data only. The combined solution of MGS, ODY and MRO data allowed us to also retrieve the time-variability of C_{50} . Figure 13-D shows the geoid heights seasonal variations associated to C_{50} , which is consistent with the results by Sanchez et al. (2006). The time-variable coefficients reported in that
805 study were determined with the NASA/Ames general circulation model, after separating the gravitational contributions of the north and south polar caps, and the atmosphere.

The global solution of C_{20} and C_{40} is significantly affected by the low signal to noise ratio that these coefficients have in the radio tracking data. C_{20}
810 shows an unexpected large amplitude of ~ 30 mm during winter in the northern hemisphere. On the other hand, the time-variable C_{40} is more stable and it is

Table 3: Estimated annual, semi-annual, and tri-annual zonal harmonic coefficients of degrees 2, 3, 4, and 5.

	Annual (k=1)		Semi-annual (k=2)		Tri-annual (k=3)	
	A	B	A	B	A	B
$\bar{C}_{20} \times 10^{-9}$	2.39 ± 0.016	-0.83 ± 0.016	1.23 ± 0.016	0.73 ± 0.016	0.53 ± 0.016	0.46 ± 0.016
$\bar{C}_{30} \times 10^{-9}$	1.67 ± 0.011	2.35 ± 0.011	0.32 ± 0.011	0.21 ± 0.011	0.13 ± 0.011	0.15 ± 0.011
$\bar{C}_{40} \times 10^{-10}$	0.85 ± 0.101	-1.56 ± 0.101	0.35 ± 0.101	-0.24 ± 0.101	-0.51 ± 0.101	-0.64 ± 0.101
$\bar{C}_{50} \times 10^{-9}$	0.38 ± 0.010	1.30 ± 0.010	0.15 ± 0.010	0.42 ± 0.010	0.32 ± 0.010	-0.02 ± 0.010

in agreement with the solution by Sanchez et al. (2006).

To further investigate these anomalously large variations in the time-variable C_{20} , we performed a mission-by-mission analysis of the time-varying gravity field. We combined arcs for each mission into monthly batches, excluding superior solar conjunctions, and we solved for all local parameters, and a series of C_{20} and C_{30} coefficients, holding all the other global parameters to their prime solution (GMM-3) values. Figure 14 shows C_{20} and C_{30} results for separate solutions with MGS, ODY and MRO data. We report the estimated values (dots), formal uncertainties (error bars) and 5-frequency fits (annual, semi-annual, tri-annual, 1/4-annual, and 1/5 annual) showing that the inter-annual changes are detectable by the three missions. Comparison of these results reveals a similar instability of the C_{20} solutions for MGS and MRO that causes larger values at $L_s \sim 300^\circ$. The MGS and MRO solutions of the even zonal harmonics are much noisier than the ODY solution, especially during the summer in the southern hemisphere. Dust storm events in that season can lead to dramatic increases of atmospheric density, which significantly perturb the orbit of those spacecraft. Therefore, the large drag perturbation during that season affects the recovery of the seasonal C_{20} with MGS and MRO. On the other hand, the estimation of C_{20} with ODY is accurate and in good agreement with the results by Konopliv et al. (2011).

The determination of the seasonal C_{30} is stable for all the three missions

confirming the results of the global estimation. Figure 14-F shows the C_{30} solution from MRO that is less noisy compared to the MGS and ODY solutions.

835 The more frequent AMDs of the latter two spacecraft affect the determination of the seasonal C_{30} although our refined modeling of ΔV s allows mitigating this perturbing effect (Konopliv et al., 2006, 2011). The exclusion of the AMDs in the MRO arcs led to precise inter-annual variations of the odd zonal harmonics. However, the main improvement in the monitoring of the seasonal gravity odd

840 harmonics with MRO radio tracking data is due to the improved atmospheric model DTM-Mars. The MRO lower altitudes cause strong drag perturbations that may compromise significantly the estimation of the time-variable gravity. But the improved modeling of the atmospheric density reduced the RMS of the range rate residuals for MGS, ODY, and especially MRO, leading to more

845 accurate orbits (Genova et al., 2015b). A future study will focus on refining the modeling of DTM-Mars seasonal atmospheric density variations and dust storms in order to stabilize the seasonal C_{20} detected using MGS and MRO data.

The consistency between MGS, ODY, and MRO solutions for C_{30} and the

850 stable ODY solution for C_{20} was used to constrain the seasonal mass variations of the polar caps. These zonal coefficients provide direct information on the solid planet and they do not need any further correction to remove the gravity contribution of the atmosphere. The time-variable gravity is almost exclusively related to CO_2 condensation and sublimation in the ice caps on a seasonal cycle.

855 We applied a point mass model at each pole (M_{NP}, M_{SP}) to recover their inter-annual mass exchange with C_{20} and C_{30} (Karatekin et al., 2005, 2006; Smith et al., 2009). The point masses in the geometric center of the polar ice caps are defined as follows:

$$\begin{aligned}
 M_{NP} &= \frac{C_{20} + C_{30}}{2} M_{Mars} \\
 M_{SP} &= \frac{C_{20} - C_{30}}{2} M_{Mars}
 \end{aligned}
 \tag{8}$$

where M_{Mars} is the total mass of Mars (Karatekin et al., 2006). Figure 15
860 shows the relative point mass variations of the polar caps during the Martian
year with the minima set to zero. Despite the simplicity of the model, the inter-
annual mass exchange between the polar caps is consistent with previous work
based on radio science data (Yoder et al., 2003; Konopliv et al., 2006; Smith
et al., 2009). The southern cap mass history displays its maximum at $\sim 8.4 \times$
865 10^{15} kg close to the autumnal equinox ($L_s=180^\circ$). The annual and inter-annual
phase is in good agreement with GCM results (Karatekin et al., 2006; Smith
et al., 2009). The north pole shows flatter mass variations during spring and
summer in the northern hemisphere compared to the previous gravity solution
by Konopliv et al. (2006) and this trend is more consistent with GCM and
870 neutron spectrometer measurements (Karatekin et al., 2006).

The continuous time-variable gravity monitoring from MGS, ODY and MRO
allows us to recover the polar caps mass history through an entire solar cycle
(~ 11 years). We focused on the inter-annual mass variation of the polar caps
from October 2002 to November 2014. The monthly estimation of C_{30} from
875 all the three spacecraft provides a sufficient sampling of the Martian seasons
through this time span. Nevertheless, the estimation of C_{20} from ODY only is
less continuous because of data gaps due to superior solar conjunctions. **Fig-
ureS4** shows ODY C_{20} and MGS, ODY and MRO C_{30} estimated values with
the 5-frequency fits (solid line) that account for solar cycle (11 and 5.5 years
880 frequencies) and inter-annual variations (annual, semiannual, and tri-annual).
These 5-frequency fit curves, which are defined by the coefficients reported in
Table 4, provide the evolution of these two zonal harmonics over the past 11
years. Therefore, we applied the point mass model to reproduce the mass ex-
change between polar caps and atmosphere from October 2002 to November
885 2014. Figure 16 shows our gravity measurement of the seasonal CO_2 masses
of the north and south poles. The pattern of deposition and sublimation is
symmetric in both hemispheres with larger amplitudes in the south.

To assess the mass exchange between the atmosphere and the polar caps, we
summed the north and south polar masses quantifying the total mass sublimed

Table 4: Coefficients of the 5-frequency fit (11-year, 5.5-year, annual, semi-annual, and tri-annual) of C_{20} from ODY only and C_{30} from MGS, ODY and MRO.

		$\bar{C}_{20} \times 10^{-9}$	$\bar{C}_{30} \times 10^{-9}$
11-years	A	-0.063 ± 0.694	0.168 ± 0.165
	B	-0.349 ± 0.700	-0.168 ± 0.198
5.5-years	A	-0.686 ± 0.633	0.002 ± 0.172
	B	-0.479 ± 0.682	0.055 ± 0.172
Annual	A	0.468 ± 0.743	-3.260 ± 0.185
	B	0.961 ± 0.579	-1.544 ± 0.172
Semi-annual	A	0.038 ± 0.646	0.621 ± 0.173
	B	1.264 ± 0.599	-0.202 ± 0.171
Tri-annual	A	-0.486 ± 0.617	-0.069 ± 0.167
	B	-0.011 ± 0.612	0.207 ± 0.174

890 into the atmosphere. Figure 17 shows the atmospheric mass variations from Mars-GRAM2010 (black dot-line, Justus and James, 2001; Justh et al., 2011) and from the negative sum of the gravity recovered masses of the polar caps (blue dot-line). These two curves highly correlate (~ 0.85), and the inter-annual mass exchange is consistent. The atmospheric mass estimated indirectly from gravity
895 shows larger variations due to the solar cycle. Despite the high uncertainties in the 11-year and 5.5-year time-variable coefficients, the larger amplitudes of the atmospheric mass in 2003 and 2013 correspond to peaks of the solar flux.

6. Summary and Conclusions

The Mars gravity field GMM-3 in spherical harmonics to degree and order
900 der 120 has been developed using the radio tracking data of the Mars Global Surveyor, Mars Odyssey, and Mars Reconnaissance Orbiter missions. The additional MRO radio tracking data from 2008 to 2015 helped refine the resolution of the gravity anomalies. GMM-3 shows a better correlation with the topography of Mars compared to previous solutions. The accurate modeling of the

905 non-conservative forces (drag, AMDs, solar radiation pressure) is the main factor for improvements in the estimation of the gravity field. The atmospheric DTM-Mars model, in particular, allowed us to enhance the orbit determination accuracy. The MRO range rate also showed systematic patterns during the re-orientation of its solar arrays. The inclusion of 1-s time series of the center of
910 mass position solved the signatures in the Doppler residuals that were due to CoM displacement of ~ 20 cm caused by the extensive areas of the solar arrays.

The maximum resolution of the gravity field is ~ 105 km in the south pole as showed by the degree strength solution. The free-air gravity anomalies are smoother compared to previous gravity fields displaying new features that correlate well with topography. The gravity trough between Acidalia Planitia and
915 Tempe Terra, which was already observed after the first MGS gravity solution, is sharp and extends from Shalbatana Vallis to Kasei Valles. This gravity anomaly may be due to the burial of a flexural moat and a low-density crustal root. We showed correlations and admittances localized over the north and south poles,
920 and the two volcanos, Olympus Mons and Elysium Mons, using a cap of 30° . The localized correlations with topography are improved with respect to previous work and the admittances provide new perspectives of the lithospheric thickness in these volcanic regions.

The estimated gravity field harmonic coefficients account only for the solid
925 planet. The gravity contribution of the atmosphere was provided separately by deriving spherical harmonics from surface pressure grids of the Mars-GRAM2010 model with $2.5^\circ \times 2.5^\circ$ spatial and 2-hour time resolution. Surface pressure grids every 2 hours allow us to take into account the diurnal and semi-diurnal atmospheric tides. Therefore, the solution of the Love number $k_2=0.1679 \pm 0.0009$
930 provides direct information of Mars solid tides caused by Phobos and the Sun.

The radio science data that we analyzed cover ~ 1.5 solar cycles that represents an unprecedented opportunity to monitor the seasonal CO_2 cycle. Previous studies showed stable solutions of time-varying C_{30} using MGS and ODY data only. We presented here the time-variable zonal harmonics with MGS,
935 ODY and MRO applying two different approaches. First, we estimated the

3-frequency (annual, semi-annual, and tri-annual) time-variable coefficients of C_{20} , C_{30} , C_{40} , and C_{50} in the global inversion. The odd zonal harmonics are stable and consistent with previous results based on gravity, neutron spectrometer, and atmospheric observations. On the other hand, the C_{20} coefficient shows
940 unexpected larger values during the summer in the southern hemisphere. Therefore, we adopted a second method to estimate the time-variable gravity by using a monthly-batch mission by mission analysis. The results demonstrated that the C_{20} instability is mainly due to MGS and MRO radio data. The ODY monthly solution indeed shows variabilities that are in good agreement with previous
945 measurements. The combination of the C_{20} solution from ODY only and C_{30} from MGS, ODY and MRO led us to determine the inter-annual mass exchange between the polar caps over ~ 11 years (from October 2002 to November 2014). The negative sum of the mass of the polar caps provides information on the atmospheric mass that is consistent with the Mars-GRAM2010 correlating at
950 ~ 0.85 .

7. Acknowledgments

This work is supported by the NASA Mars Reconnaissance Orbiter Radio Science Investigation. We are grateful to Jean-Paul Boy (Ecole et Observatoire des Sciences de la Terre, Strasbourg, France) for helping this research by providing
955 detailed information on the gravity contribution of the atmosphere. We thank David Rowlands (NASA, GSFC) for his help with the GEODYN software. The data used in this paper are available at <http://geo.pds.nasa.gov/>. S. Goossens was supported by NASA grant NNX09AO75G.

References

- 960 Asmar, S., Armstrong, J., Iess, L., Tortora, P., 2005. Spacecraft Doppler tracking: Noise budget and accuracy achievable in precision radio science observations. *Radio Sci.* 40.

- Belleguic, V., Lognonné, P., Wieczorek, M., 2005. Constraints on the martian lithosphere from gravity and topography data. *J. Geophys. Res.: Planets* (1991–2012) 110.
- 965
- Bills, B.G., Neumann, G.A., Smith, D.E., Zuber, M.T., 2005. Improved estimate of tidal dissipation within Mars from MOLA observations of the shadow of Phobos. *J. Geophys. Res.: Planets* (1991–2012) 110.
- Boy, J.P., Chao, B.F., 2005. Precise evaluation of atmospheric loading effects on Earth’s time-variable gravity field. *J. Geophys. Res.: Solid Earth* (1978–2012)
- 970 110.
- Boy, J.P., Gegout, P., Hinderer, J., 2002. Reduction of surface gravity data from global atmospheric pressure loading. *Geophys. J. Int.* 149, 534–545.
- Boy, J.P., Hinderer, J., Gegout, P., 1998. Global atmospheric loading and gravity. *Physics of the Earth and Planetary Interiors* 109, 161–177.
- 975
- Boy, J.P., Petrov, L., 2005. Memo on computing Stokes coefficients of the expansion of the atmosphere contribution to the geopotential into a series of spherical harmonics. URL: http://gemini.gsfc.nasa.gov/agra/agra_memo_01.ps.
- Bruinsma, S., Lemoine, F.G., 2002. A preliminary semiempirical thermosphere
- 980 model of Mars: DTM-Mars. *J. Geophys. Res.: Planets* (1991–2012) 107, 15–1.
- Cheng, M., Tapley, B.D., Ries, J.C., 2013. Deceleration in the earth’s oblateness. *J. Geophys. Res.: Solid Earth* 118, 740–747.
- Cutting, E., Frautnick, J., Born, G., 1978. Orbit analysis for SEASAT-A. *J. Astronaut. Sci.* 26, 315–342.
- 985
- Defraigne, P., Viron, O.d., Dehant, V., Van Hoolst, T., Hourdin, F., 2000. Mars rotation variations induced by atmosphere and ice caps. *J. Geophys. Res.: Planets* (1991–2012) 105, 24563–24570.

- Demmel, J., 1997. Applied Numerical Linear Algebra. Society for Industrial and
990 Applied Mathematics, Philadelphia, PA. doi:10.1137/1.9781611971446.
- Dombard, A.J., Searls, M.L., Phillips, R.J., 2004. An alternative explanation
for the “buried channels” on Mars: The gravity signal from a sharp boundary
on partially compensated, long-wavelength topography. *Geophys. Res. Let.*
31.
- 995 Fishbaugh, K.E., Head, J.W., 2001. Comparison of the north and south po-
lar caps of Mars: New observations from mola data and discussion of some
outstanding questions. *Icarus* 154, 145–161.
- Folkner, W.M., Williams, J.G., Boggs, D.H., 2008. The planetary and lunar
ephemeris DE 421. IPN Progress Report , 42–178.
- 1000 Gaposchkin, E., Coster, A., 1986. Evaluation of recent atmospheric density
models. *Advances in space research* 6, 157–165.
- Gaposchkin, E.M., Coster, A.J., 1988. Analysis of satellite drag. Technical
Report. Massachusetts Inst. of Tech., Lexington (USA). Lincoln Lab.
- Genova, A., Goossens, S., Lemoine, F., Mazarico, E., Smith, D., Zuber, M.,
1005 2015a. The Gravity Field of Mars from MGS, Mars Odyssey, and MRO
Radio Science, in: *Lunar Planet. Sci. Conf.*, p. 1872.
- Genova, A., Goossens, S., Lemoine, F.G., Mazarico, E., Fricke, S.K., Smith,
D.E., Zuber, M.T., 2015b. Long-term variability of CO₂ and O in the Mars
upper atmosphere from MRO radio science data. *J. Geophys. Res.: Planets*
1010 120, 849–868. doi:10.1002/2014JE004770.
- Iess, L., Di Benedetto, M., James, N., Mercolino, M., Simone, L., Tortora,
P., 2014. Astra: Interdisciplinary study on enhancement of the end-to-end
accuracy for spacecraft tracking techniques. *Acta Astronautica* 94, 699–707.
- Jacobson, R.A., 2010. The orbits and masses of the Martian satellites and the
1015 libration of Phobos. *Astronom. J.* 139, 668.

- Jeffreys, H., 1959. The reduction of gravity observations. *Geophys. J. Int.* 2, 42–44.
- Justh, H., Justus, C., Ramey, H., 2011. Mars-GRAM 2010: improving the precision of Mars-GRAM. *Mars Atmosphere: Modelling and observation 1*, 265–267.
- 1020
- Justus, C.G., James, B., 2001. Mars Global Reference Atmospheric Model 2001 Version (Mars-GRAM 2001): Users Guide. volume 210961. National Aeronautics and Space Administration, Marshall Space Flight Center.
- Justus, C.G., Johnson, D.L., James, B., 1996. A Revised Thermosphere for the Mars Global Reference Atmospheric Model (Mars-GRAM Version 3.4). volume 108513. National Aeronautics and Space Administration, Marshall Space Flight Center.
- 1025
- Karatekin, Ö., Duron, J., Rosenblatt, P., Van Hoolst, T., Dehant, V., Barriot, J.P., 2005. Mars’ time-variable gravity and its determination: Simulated geodesy experiments. *J. Geophys. Res.: Planets* (1991–2012) 110.
- 1030
- Karatekin, Ö., Van Hoolst, T., Dehant, V., 2006. Martian global-scale CO₂ exchange from time-variable gravity measurements. *J. Geophys. Res.: Planets* (1991–2012) 111.
- Kaula, W.M., 2000. Theory of satellite geodesy: applications of satellites to geodesy. Courier Corporation.
- 1035
- Konopliv, A., Banerdt, W., Sjogren, W., 1999. Venus gravity: 180th degree and order model. *Icarus* 139, 3–18.
- Konopliv, A.S., 2012. http://pds-geosciences.wustl.edu/mro/mro-m-rss-5-sdp-v1/mrors_1xxx/data/shadr/jgmro_110c_sha.1bl.
- 1040
- NASA PDS .
- Konopliv, A.S., Asmar, S.W., Folkner, W.M., Karatekin, Ö., Nunes, D.C., Smrekar, S.E., Yoder, C.F., Zuber, M.T., 2011. Mars high resolution gravity

fields from MRO, Mars seasonal gravity, and other dynamical parameters. *Icarus* 211, 401–428.

1045 Konopliv, A.S., Park, R.S., Yuan, D.N., Asmar, S.W., Watkins, M.M., Williams, J.G., Fahnestock, E., Kruizinga, G., Paik, M., Strelakov, D., et al., 2013. The JPL lunar gravity field to spherical harmonic degree 660 from the GRAIL primary mission. *J. Geophys. Res.: Planets* 118, 1415–1434.

Konopliv, A.S., Yoder, C.F., Standish, E.M., Yuan, D.N., Sjogren, W.L., 2006. 1050 A global solution for the Mars static and seasonal gravity, Mars orientation, Phobos and Deimos masses, and Mars ephemeris. *Icarus* 182, 23–50.

Lainey, V., Dehant, V., Pätzold, M., 2007. First numerical ephemerides of the martian moons. *Astronomy & Astrophysics* 465, 1075–1084.

Lemoine, F., Bruinsma, S., Chinn, D., Forbes, J., 2006. Thermospheric studies 1055 with Mars Global Surveyor, in: *AIAA/AAS Astrodynamics Specialist Conference*, Keystone, CO. Paper AIAA, pp. 1–13.

Lemoine, F., Smith, D., Lerch, F., Zuber, M., Patel, G., 1994. Progress in the development of the GMM-2 gravity field model for Mars, in: *Lunar Planet. Sci. Conf.*, pp. 789–790.

1060 Lemoine, F.G., 2009. http://pds-geosciences.wustl.edu/mro/mro-m-rss-5-sdp-v1/mrors_1xxx/data/shadr/ggmro_095a_sha.1bl. NASA PDS .

Lemoine, F.G., Chinn, D.S., Zelensky, N.P., Beall, J.W., Melachroinos, S., 2014. 1065 Time-variable Gravity Solutions from 1993 to 2013 from SLR and DORIS data, in: *EGU General Assembly Conference Abstracts*, p. 13971.

Lemoine, F.G., Goossens, S., Sabaka, T.J., Nicholas, J.B., Mazarico, E., Rowlands, D.D., Loomis, B.D., Chinn, D.S., Caprette, D.S., Neumann, G.A., et al., 2013. High-degree gravity models from GRAIL primary mission data. *J. Geophys. Res.: Planets* 118, 1676–1698.

- 1070 Lemoine, F.G., Smith, D.E., Rowlands, D.D., Zuber, M., Neumann, G., Chinn,
D., Pavlis, D., 2001. An improved solution of the gravity field of Mars (GMM-
2B) from Mars Global Surveyor. *J. Geophys. Res.: Planets* (1991–2012) 106,
23359–23376.
- Marty, J., Balmino, G., Duron, J., Rosenblatt, P., Le Maistre, S., Rivoldini, A.,
1075 Dehant, V., Van Hoolst, T., 2009. Martian gravity field model and its time
variations from MGS and Odyssey data. *Planet. Space Sci.* 57, 350–363.
- Mazarico, E., Genova, A., Goossens, S., Lemoine, F.G., Neumann, G.A., Zuber,
M.T., Smith, D.E., Solomon, S.C., 2014. The gravity field, orientation, and
ephemeris of Mercury from MESSENGER observations after three years in
1080 orbit. *J. Geophys. Res.: Planets* 119, 2417–2436. URL: [http://dx.doi.org/
10.1002/2014JE004675](http://dx.doi.org/10.1002/2014JE004675), doi:10.1002/2014JE004675.
- Mazarico, E., Zuber, M.T., Lemoine, F.G., Smith, D.E., 2007. Martian exo-
spheric density using Mars Odyssey radio tracking data. *J. Geophys. Res.:
Planets* 112, 2156–2202. doi:10.1029/2006JE002734.
- 1085 Mazarico, E., Zuber, M.T., Lemoine, F.G., Smith, D.E., 2009. Effects of self-
shadowing on nonconservative force modeling for Mars-orbiting spacecraft. *J.
Spacecraft Rockets* 46, 662–669.
- McCarthy, D.D., Petit, G., 2004. IERS conventions (2003). IERS Technical
Nore; 32 127 pp. DTIC Document. Frankfurt am Main: Verlag des Bunde-
1090 samts für Kartographie und Geodäsie, 2004.
- McGovern, P.J., Solomon, S.C., Smith, D.E., Zuber, M.T., Simons, M., Wic-
zorek, M.A., Phillips, R.J., Neumann, G.A., Aharonson, O., Head, J.W.,
2002. Localized gravity/topography admittance and correlation spectra on
Mars: Implications for regional and global evolution. *J. Geophys. Res.: Plan-
1095 ets* (1991–2012) 107, 19–1.
- McKenzie, D., Barnett, D.N., Yuan, D.N., 2002. The relationship between

- martian gravity and topography. *Earth and Planetary Science Letters* 195, 1–16.
- Métivier, L., Karatekin, Ö., Dehant, V., 2008. The effect of the internal structure of Mars on its seasonal loading deformations. *Icarus* 194, 476–486. 1100
- Millour, E., Forget, F., Lewis, S.R., 2015. Mars Climate Database v5.2 User Manual. URL: http://www-mars.lmd.jussieu.fr/mars/info_web/user_manual_5.2.pdf.
- Neumann, G.A., Zuber, M.T., Wieczorek, M.A., McGovern, P.J., Lemoine, F.G., Smith, D.E., 2004. The crustal structure of Mars from gravity and topography. *J. Geophys. Res.* 109, 2004JE002262. doi:10.1029/2004JE002262. 1105
- Pavlis, D.E., Wimert, J., McCarthy, J.J., 2013. GEODYN II System Description. vols. 1-5 ed. SGT Inc.. Greenbelt, MD.
- Petrov, L., Boy, J.P., 2004. Study of the atmospheric pressure loading signal in very long baseline interferometry observations. *J. Geophys. Res.: Solid Earth* (1978–2012) 109. 1110
- Phillips, R., Saunders, R., 1975. The isostatic state of martian topography. *J. Geophys. Res.* 80, 2893–2898.
- Phillips, R., Sjogren, W., Johnson, C., 1999. The mystery of the Mars north polar gravity-topography correlation (or lack thereof), in: *The Fifth Int. Conf. on Mars*, p. 6118. 1115
- Phillips, R.J., Zuber, M.T., Solomon, S.C., Golombek, M.P., Jakosky, B.M., Banerdt, W.B., Williams, R.M.E., Hynek, B.M., Aharonson, O., II, S.A.H., 2001. Ancient geodynamics and global-scale hydrology on Mars. *Science* 291, 2587–2591. 1120
- Rainey, E., Aharonson, O., 2006. Estimate of tidal Q of Mars using MOC observations of the shadow of Phobos, in: *The 37th Annual Lunar Planet. Sci. Conf.*, 13-17 March 2006.

- Rowlands, D., Luthcke, S., McCarthy, J., Klosko, S., Chinn, D., Lemoine, F.,
1125 Boy, J.P., Sabaka, T., 2010. Global mass flux solutions from GRACE: a
comparison of parameter estimation strategies—mass concentrations versus
Stokes coefficients. *J. Geophys. Res.: Solid Earth (1978–2012)* 115.
- Runcorn, S., 1965. Changes in the convection pattern in the earth's mantle
and continental drift: evidence for a cold origin of the earth. *Philosophical*
1130 *Transactions of the Royal Society of London A: Mathematical, Physical and*
Engineering Sciences 258, 228–251.
- Sanchez, B.V., Rowlands, D.D., Haberle, R.M., 2006. Variations of Mars
gravitational field based on the NASA/Ames general circulation model.
J. Geophys. Res.: Atmospheres (1991–2012) 111, E06010. doi:10.1029/
1135 2005JE002442.
- Saunders, R., Arvidson, R., Badhwar, G., Boynton, W., Christensen, P., Cucinotta, F., Feldman, W., Gibbs, R., Kloss Jr, C., Landano, M., et al., 2004. 2001 Mars Odyssey mission summary, in: *2001 Mars Odyssey*. Springer, pp. 1–36.
- 1140 Sigurdsson, H., Houghton, B., McNutt, S., Rymer, H., Stix, J. (Eds.), 2015. *The Encyclopedia of Volcanoes*. Second ed.. Elsevier. chapter 41. pp. 721–723.
- Simons, M., Solomon, S.C., Hager, B.H., 1997. Localization of gravity and topography: Constraints on the tectonics and mantle dynamics of venus. *Geophys. J. Int.* 131, 24–44.
- 1145 Smith, D., Lerch, F., Nerem, R., Zuber, M., Patel, G., Fricke, S., Lemoine, F., 1993. An Improved Gravity Model for Mars: Goddard Mars Model–1 (GMM–1). Goddard Space Flight Center.
- Smith, D.E., Sjogren, W.L., Tyler, G.L., Balmino, G., Lemoine, F.G., Konopliv, A.S., 1999a. The gravity field of Mars: results from Mars Global Surveyor.
1150 *Science* 286, 94–97.

- Smith, D.E., Zuber, M.T., Frey, H.V., Garvin, J.B., Head, J.W., Muhleman, D.O., Pettengill, G.H., Phillips, R.J., Solomon, S.C., Zwally, H.J., et al., 2001. Mars Orbiter Laser Altimeter: Experiment summary after the first year of global mapping of Mars. *J. Geophys. Res.: Planets* (1991–2012) 106, 23689–23722.
- 1155
- Smith, D.E., Zuber, M.T., Solomon, S.C., Phillips, R.J., Head, J.W., Garvin, J.B., Banerdt, W.B., Muhleman, D.O., Pettengill, G.H., Neumann, G.A., et al., 1999b. The global topography of Mars and implications for surface evolution. *Science* 284, 1495–1503.
- 1160
- Smith, D.E., Zuber, M.T., Torrence, M.H., Dunn, P.J., Neumann, G.A., Lemoine, F.G., Fricke, S.K., 2009. Time variations of Mars’ gravitational field and seasonal changes in the masses of the polar ice caps. *J. Geophys. Res.: Planets* (1991–2012) 114.
- 1165
- Smith, M.D., 2009. THEMIS observations of Mars aerosol optical depth from 2002–2008. *Icarus* 202, 444–452.
- Tanaka, K., Skinner, J., Hare, T., Joyal, T., Wenker, A., 2003. Resurfacing history of the northern plains of Mars based on geologic mapping of Mars Global Surveyor data. *J. Geophys. Res.: Planets* (1991–2012) 108.
- 1170
- Tapley, B.D., Schutz, B.E., Born, G.H., 2004. *Statistical Orbit Determination*. Elsevier, Boston, Mass.
- Tolson, R., Dwyer, A., Hanna, J., Keating, G., George, B., Escalera, P., Werner, M., 2005. Application of accelerometer data to Mars Odyssey aerobraking and atmospheric modeling. *J. Spacecraft Rockets* 42, 435–443.
- 1175
- Tolson, R., Keating, G., Cancro, G., Parker, J., Noll, S., Wilkerson, B., 1999. Application of accelerometer data to Mars Global Surveyor aerobraking operations. *J. Spacecraft Rockets* 36, 323–329.
- Tolson, R.H., Bemis, E., Zaleski, K., Keating, G., Shidner, J.D., Brown, S., Brickler, A., Scher, M., Thomas, P., Hough, S., 2008. Atmospheric modeling

- using accelerometer data during Mars Reconnaissance Orbiter aerobraking
1180 operations. *J. Spacecraft Rockets* 45, 511–518.
- Watts, A., Daly, S., 1981. Long wavelength gravity and topography anomalies. *Annual Review of Earth and Planetary Sciences* 9, 415–448.
- Werner, S.C., 2009. The global martian volcanic evolutionary history. *Icarus* 201, 44–68.
- 1185 Wicczorek, M.A., 2007. The gravity and topography of the terrestrial planets. *Treatise on Geophysics*.–2007.–10 , 165–206.
- Wicczorek, M.A., Phillips, R.J., 1998. Potential anomalies on a sphere: Applications to the thickness of the lunar crust. *J. Geophys. Res.: Planets* (1991–2012) 103, 1715–1724.
- 1190 Wicczorek, M.A., Simons, F.J., 2005. Localized spectral analysis on the sphere. *Geophys. J. Int.* 162, 655–675.
- Wicczorek, M.A., Zuber, M.T., 2004. The thickness of the Martian crust: Improved constraints from geoid-to-topography ratios. *J. Geophys. Res.* 109. doi:10.1029/2003JE002153.
- 1195 Williams, D.A., Greeley, R., Fergason, R.L., Kuzmin, R., McCord, T.B., Combe, J.P., Head, J.W., Xiao, L., Manfredi, L., Poulet, F., et al., 2009. The circum-Hellas volcanic province, Mars: overview. *Planet. Space Sci.* 57, 895–916.
- Williams, J.P., Nimmo, F., Moore, W.B., Paige, D.A., 2008. The formation of Tharsis) on Mars: What the line-of-sight gravity is telling us. *J. Geophys. Res.: Planets* (1991–2012) 113.
1200
- Wood, S.E., Paige, D.A., 1992. Modeling the martian seasonal co₂ cycle 1. fitting the viking lander pressure curves. *Icarus* 99, 1–14.
- Yin, A., 2012. Structural analysis of the valles marineris fault zone: Possible evidence for large-scale strike-slip faulting on mars. *Lithosphere* 4, 286–330.

- 1205 Yoder, C.F., Konopliv, A.S., Yuan, D.N., Standish, E.M., Folkner, W.M., 2003. Fluid Core Size of Mars from Detection of the Solar Tide. *Science* 300, 5617, 299–303. doi:10.1126/science.1079645.
- You, T.H., Halsell, A., Graat, E., Demcak, S., Highsmith, D., Long, S., Bhat, R., Mottinger, N., Higa, E., Jah, M., 2007. Mars Reconnaissance Orbiter
1210 interplanetary cruise navigation, in: 20th Int. Symp. on Space Flight Dyn., Annapolis, MD, Citeseer. pp. 1–16.
- Yuan, D.N., Sjogren, W.L., Konopliv, A.S., Kucinskas, A.B., 2001. Gravity field of Mars: a 75th degree and order model. *J. Geophys. Res.: Planets* (1991–2012) 106, 23377–23401.
- 1215 Zuber, M.T., Lemoine, F.G., Smith, D.E., Konopliv, A.S., Smrekar, S.E., Asmar, S.W., 2007. Mars Reconnaissance Orbiter radio science gravity investigation. *J. Geophys. Res.: Planets* 112, E05S07. doi:10.1029/2006JE002833.
- Zuber, M.T., Solomon, S.C., Phillips, R.J., Smith, D.E., Tyler, G.L., Aharonson, O., Balmino, G., Banerdt, W.B., Head, J.W., Johnson, C.L., et al., 2000.
1220 Internal structure and early thermal evolution of Mars from Mars Global Surveyor topography and gravity. *Science* 287, 1788–1793.

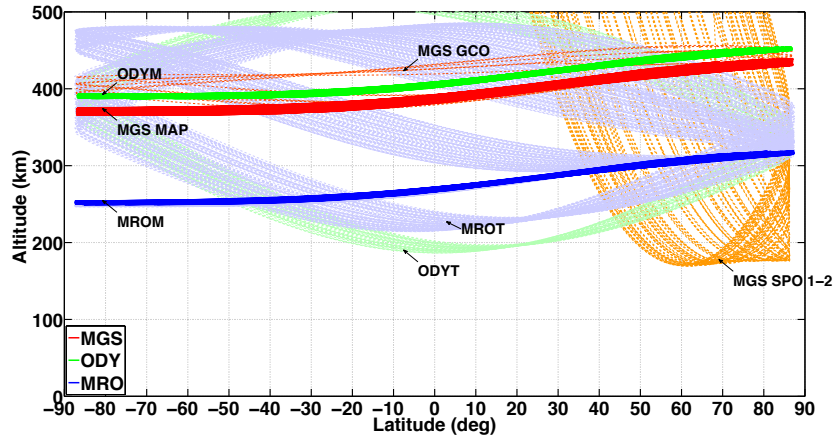


Figure 1: MGS, Mars Odyssey, and MRO latitude and geodetic altitude coverage in orbit about Mars.

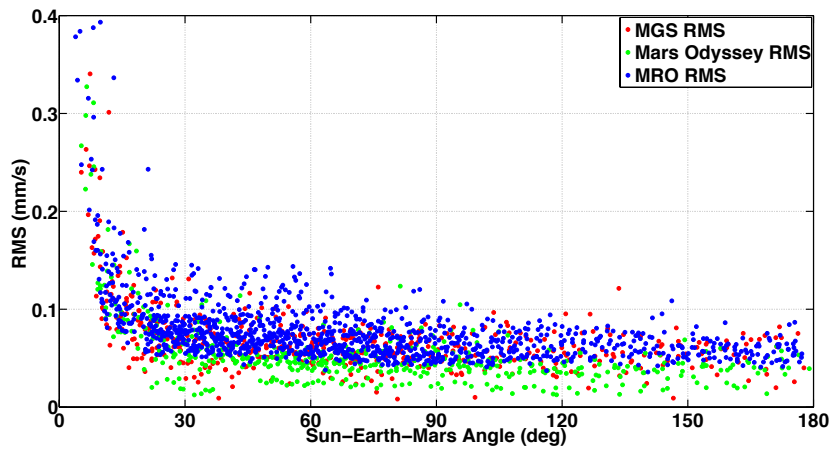


Figure 2: 2-way Doppler data fit of MGS (red), ODY (green), and MRO (blue) with respect to the SEP angle. These values are over a count interval of 60 s, but the data used in our solution are sampled at 10 s.

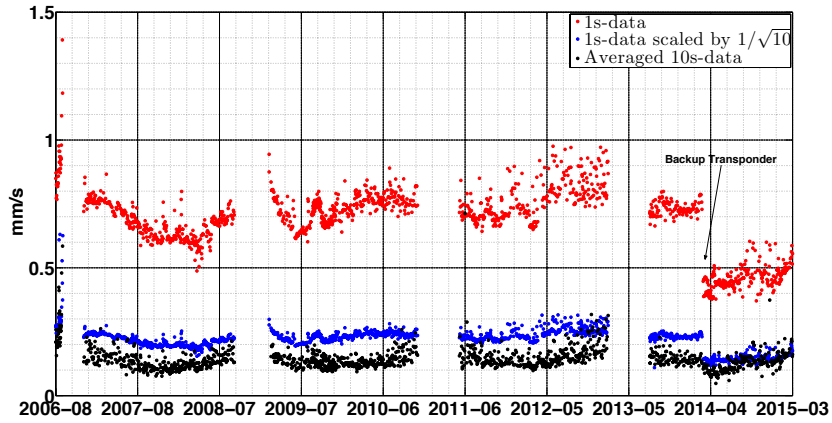


Figure 3: MRO 2-way range rate data for a count interval of 1 s (red dots) and 10 s (black dots). We scaled the 1-s data to a 10-s integration time (blue dots) applying a scatter reduction of $1/\sqrt{10}$ to compare the quality of the two averaging times.

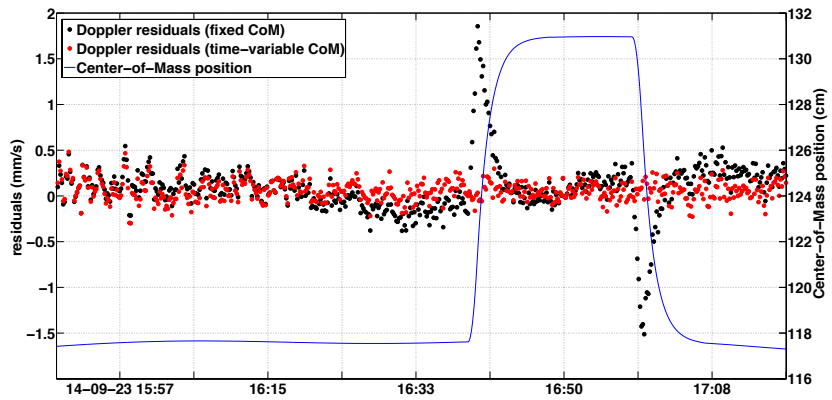


Figure 4: MRO 2-way range rate residuals of 23 September 2014 with (red) and without (black) correction of the center of mass position (blue line). Rapid movement of the MRO solar arrays, which have an extensive areas ($\sim 10 \text{ m}^2$), displace the spacecraft center-of-mass by $\sim 20\text{cm}$ resulting in erroneous apparent range rates.

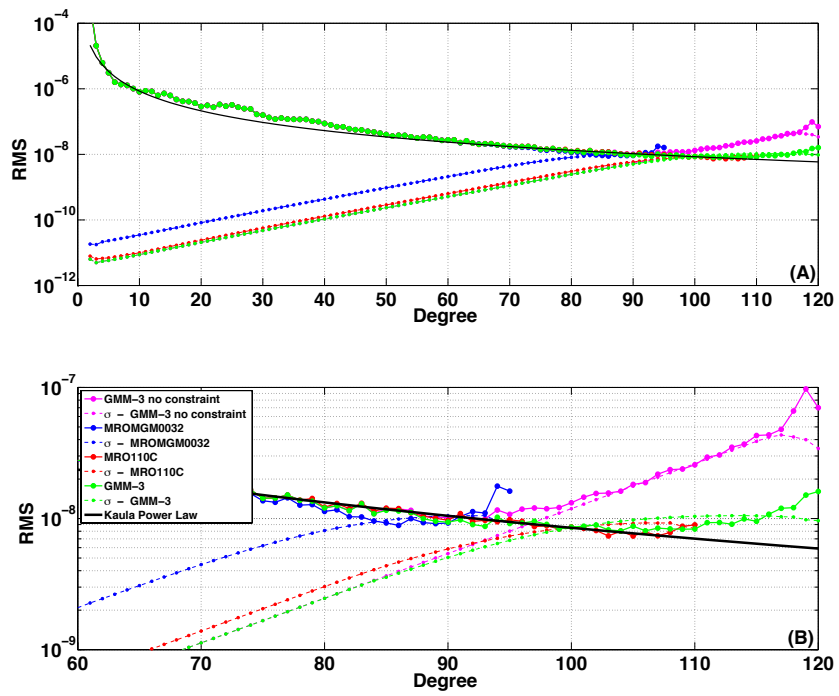


Figure 5: Total power (A) and higher degree spectra (B) of the GMM-3, MRO110C, and MROMGM0032 solutions and relative formal uncertainties.

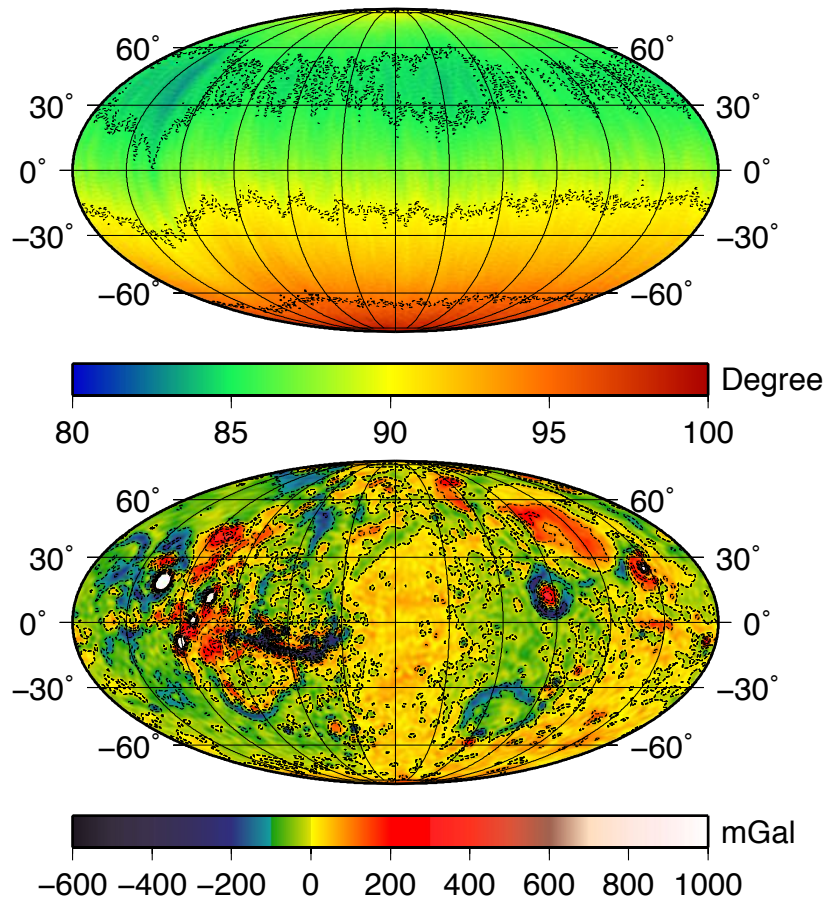


Figure 6: GMM-3 degree strength (top) computed with gravity accelerations that follow the power rule $8.5 \times 10^{-4}/l^2$ and the full covariance matrix. GMM-3 free-air gravity anomaly map (bottom) expanded at each point only up to its specific degree strength.

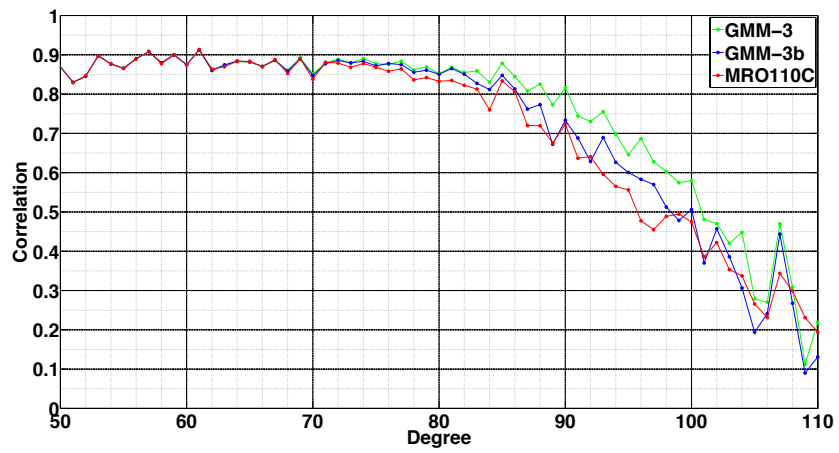


Figure 7: Correlation between the MOLA topographic-based gravity field and the three gravity solutions GMM-3 (green), MRO110C (red), and GMM-3b (blue), which is based on the same dataset used for MRO110C.

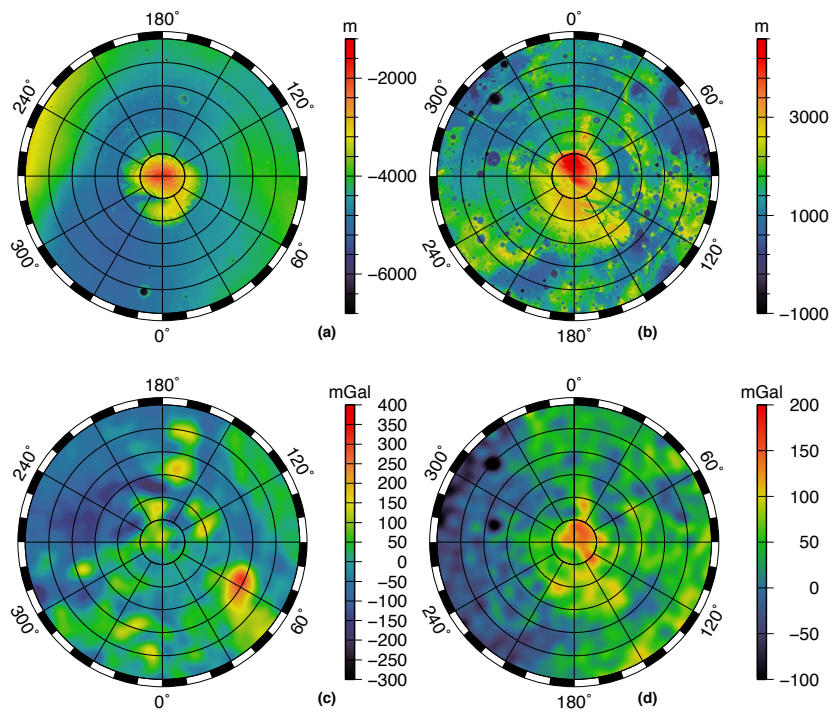


Figure 8: Maps in stereographic projection centered at the north (left panels, 60°N - 90°N) and south pole (right panels, 60°S - 90°S) for MOLA topography (a,b) and free-air degree strength gravity anomalies (c,d).

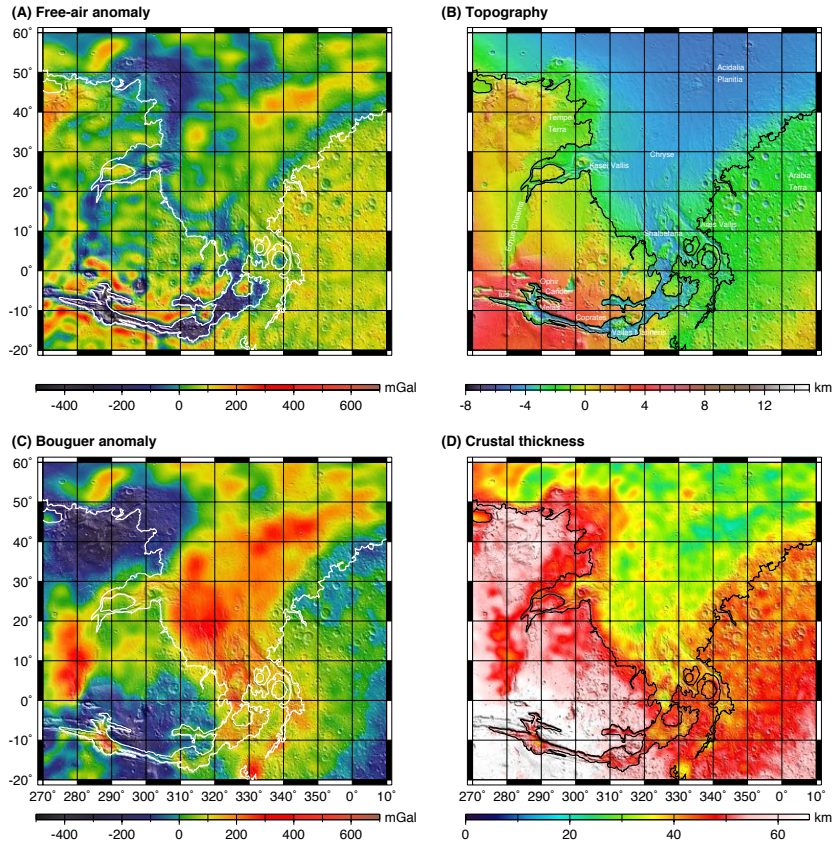


Figure 9: (a) Free-air degree strength gravity anomalies (b) MOLA topography (c) Bouguer gravity anomaly and (d) crustal thickness, over a portion of the western hemisphere. A topographic contour (white or black curve) at -1800 m in the west and dipping 0.02° toward the East is explained in the text.

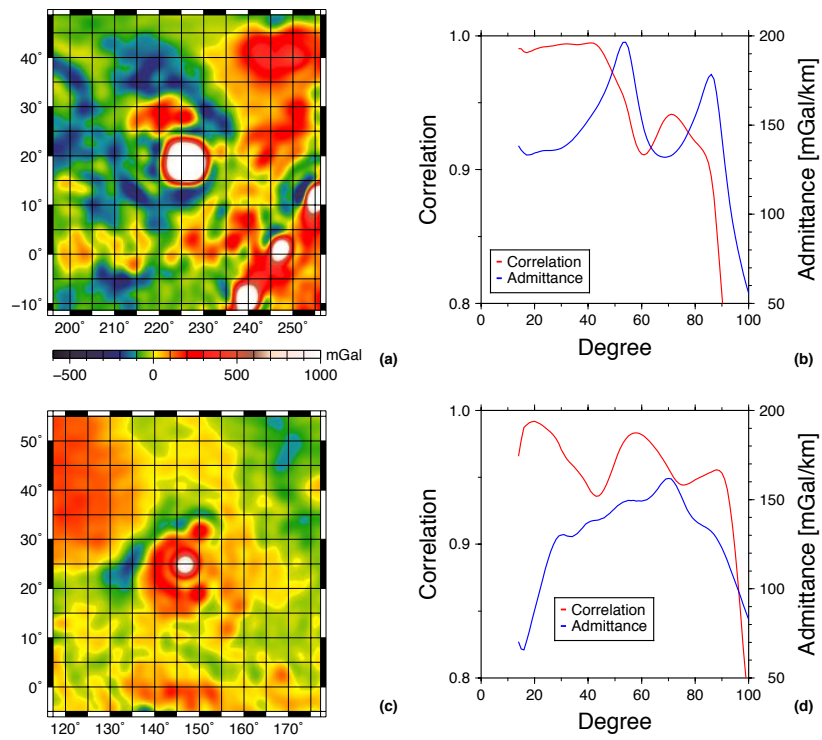


Figure 10: Free-air degree strength gravity anomalies (a,c), correlation and admittance spectra between GMM-3 gravity and MOLA topography (b,d) for Olympus Mons (19°N, 226°E) and Elysium Mons (19°N, 226°E).

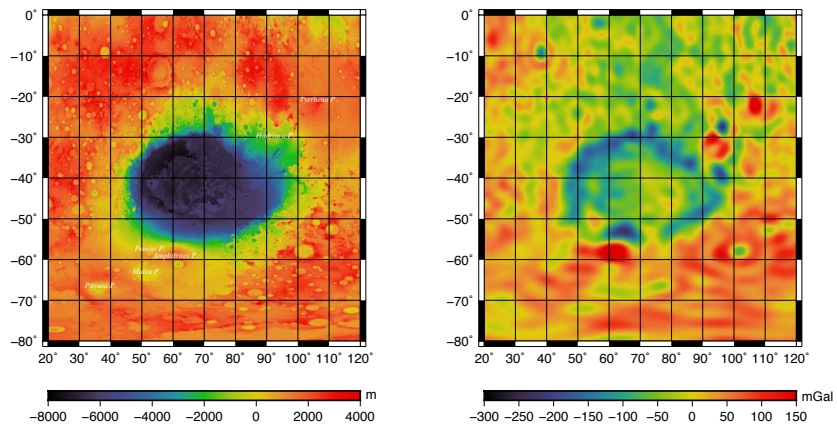


Figure 11: MOLA topography (left) and free-air degree strength gravity anomalies (right) over the Hellas basin and the Circum-Hellas Volcanic Province.

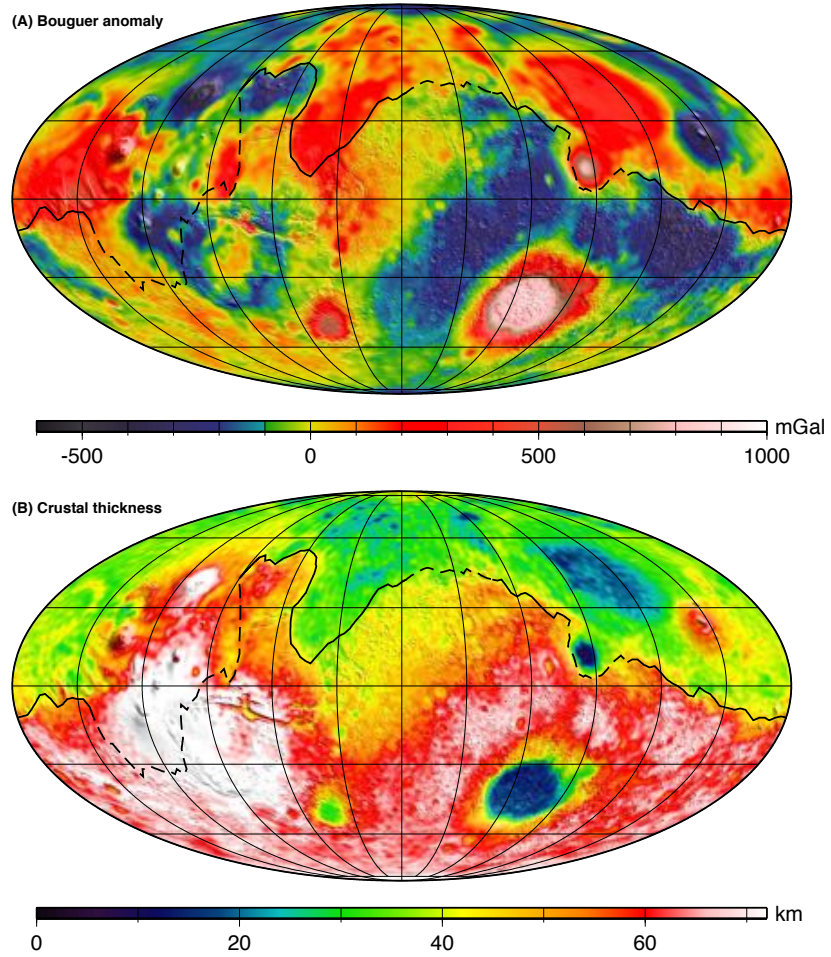


Figure 12: (a) Global Bouguer anomaly and (b) crustal thickness over shaded relief.

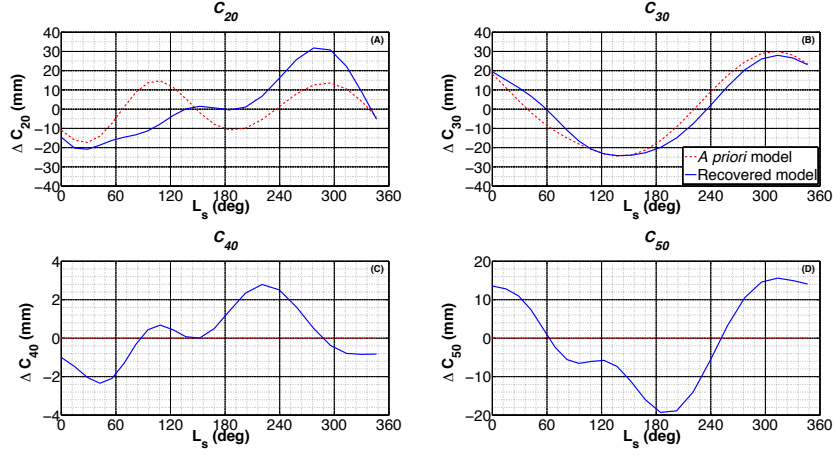


Figure 13: Time-variable zonal harmonics C_{20} (A), C_{30} (B), C_{40} (C), and C_{50} (D) versus L_s derived globally with MGS, ODY and MRO. Three frequencies (annual, semi-annual, and tri-annual) have been included in the adjustments providing direct measurement of the inter-annual mass exchange of the solid planet.

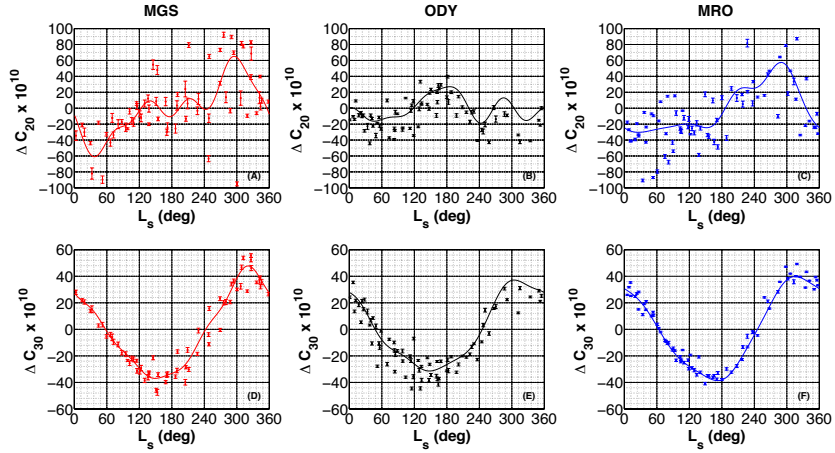


Figure 14: C_{20} and C_{30} solutions and uncertainties in a monthly mission by mission estimation. Solid lines represent a 5 frequency fit of C_{20} and C_{30} solutions. MGS results are in red (A-D), ODY in black (B-E), and MRO in blue (C-F).

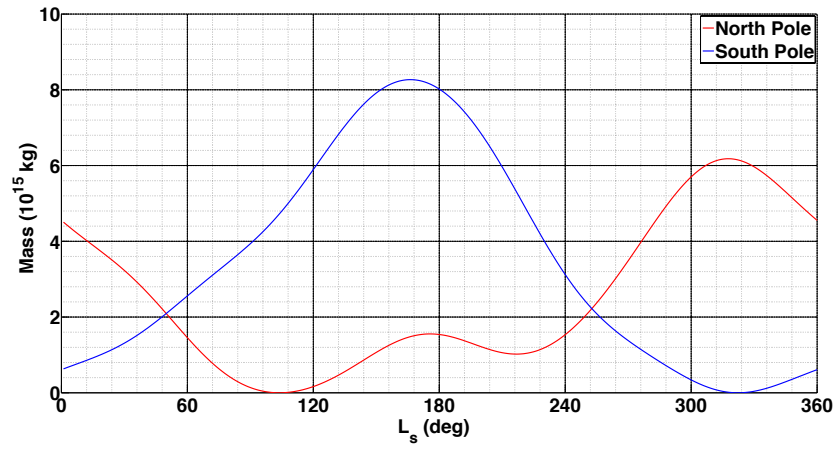


Figure 15: Mass variation of the north (red) and south (blue) polar caps using point mass model with C_{20} and C_{30} time series derived from ODY only, and MGS, ODY and MRO solutions, respectively. The minima were set to zero in order to look at relative changes.

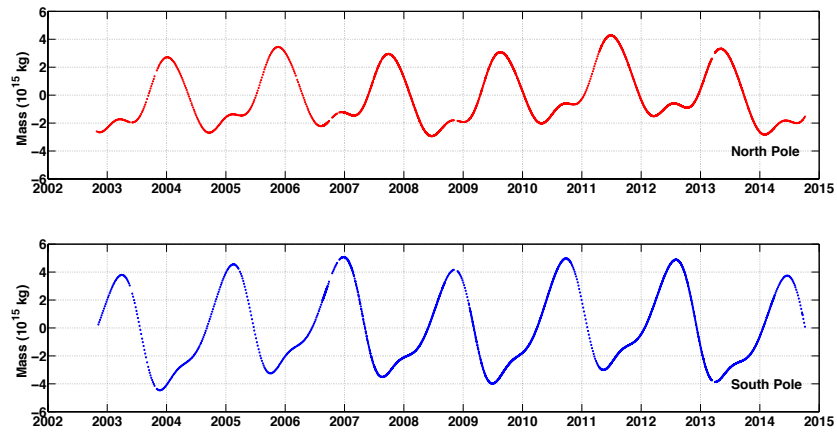


Figure 16: Mass values of the north and south seasonal caps derived by assuming a point mass model with C_{20} and C_{30} time-series (**FigureS4**).

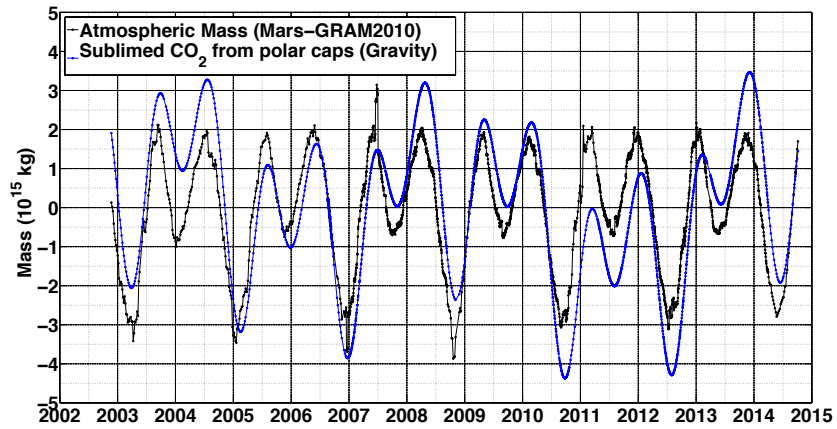


Figure 17: Atmospheric mass variations over the last 11 years retrieved with Mars-GRAM2010 pressure fields (black dot-line), and with gravity measured mass exchanges between the polar caps.